Marine Chemistry 257 (2023) 104330

Contents lists available at ScienceDirect

Marine Chemistry

journal homepage: www.elsevier.com/locate/marchem

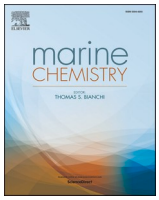

Variability in zinc:phosphorous and zinc:silicon ratios and zinc isotope fractionation in Southern Ocean diatoms: Observations from laboratory and field experiments

Robin Grun [a], Moneesha Samanta [a], Michael J. Ellwood [a,b,*]

[a] Research School of Earth Sciences, Australian National University, ACT, Australia
[b] Australian Centre for Excellence in Antarctic Science, Research School of Earth Sciences, Australian National University, ACT, Australia

ARTICLE INFO

Keywords:
Southern Ocean
Phytoplankton
Zinc isotopes
Zinc quota
Iron limitation

ABSTRACT

We studied the impact of iron limitation on zinc uptake and the zinc isotope ($\delta^{66}Zn$) composition for Southern Ocean phytoplankton. We undertook laboratory culture and field incubation experiments, and linked these to *in situ* depth profiles of dissolved (dZn) and particulate (pZn) zinc collected from three sites in the Southern Ocean. For the laboratory experiments, diatom growth rates, cellular zinc accumulation, and $\delta^{66}Zn$ all responded to changes in iron and zinc bioavailability. A significant increase in the cellular quota for zinc (expressed as zinc:phosphorous (Zn:P)) occurred upon iron limitation and zinc enrichment. At the same time, $\delta^{66}Zn$ for organic tissues became isotopically light under high zinc and low iron concentrations. The opposite occurred for frustule $\delta^{66}Zn$ values. Here $\delta^{66}Zn_{frustule\text{-}organic}$ for cultured phytoplankton became isotopically heavier under high zinc and low iron concentrations. For senescing and dead cells, Zn:P declined and $\delta^{66}Zn$ increased, indicating a loss of isotopically light zinc from organic matter. For field incubation experiments, $\delta^{66}Zn_{frustule}$ was isotopically heavier than seawater, except for added zinc treatments. The percentage of zinc associated with frustule material for laboratory and field incubations encompassed a wide range with values between 1 and 57%. Depth profiles of $\delta^{66}Zn$ for dZn and pZn varied, with dZn being isotopically lighter than pZn in low dZn concentration subantarctic waters, whereas the opposite occurred in polar waters where dZn was isotopically heavier than pZn at higher dZn concentrations. Our results show that iron and zinc availability regulates the zinc content of phytoplankton and the $\delta^{66}Zn$ composition of the Southern Ocean, which is propagated to other parts of the world ocean.

1. Introduction

The Southern Ocean plays a significant role in the global carbon cycle, influencing both ocean circulation and biogeochemistry (Rintoul, 2018). This influence results from its central role in ocean circulation by connecting the Atlantic, Indian, and Pacific oceans. The Southern Ocean also plays a crucial role in controlling many global oceanic processes (e.g. formation of the Antarctic Intermediate Waters and the Subantarctic Mode Waters), which are reflected in other parts of the global ocean (Rintoul, 2018; Sarmiento et al., 2004). Thus, the processes that influence the biogeochemical composition of surface waters of the Southern Ocean are reflected in other parts of the world ocean via these water masses.

For large swaths of the Southern Ocean, phytoplankton growth is sub-optimal because of limited iron supply to surface waters (e.g. Boyd et al., 2000; Coale et al., 2004). The Southern Ocean is geographically isolated and consequently has low aeolian dust deposition and riverine or sedimentary source iron inputs, which, combined with its chemical speciation and the dominance of insoluble iron species, makes bioavailable iron a limiting growth factor for many phytoplankton (Boyd and Ellwood, 2010; Deppeler and Davidson, 2017). Iron limitation of Southern Ocean phytoplankton also weakens the efficiency of the biological carbon pump and influences nutrient utilisation by phytoplankton. Increased phytoplankton productivity has been observed in some areas of the Southern Ocean, where iron concentrations are elevated due to the resuspension of continental shelf sediments and/or meltwater input from sea ice (Graham et al., 2015).

Zinc is another important trace metal micronutrient because it acts as a cofactor in several important enzymes within phytoplankton, including carbonic anhydrase, alkaline phosphatase, RNA polymerase,

* Corresponding author at: Research School of Earth Sciences, Australian National University, ACT, Australia.
E-mail address: michael.ellwood@anu.edu.au (M.J. Ellwood).

https://doi.org/10.1016/j.marchem.2023.104330
Received 21 November 2022; Received in revised form 9 August 2023; Accepted 28 October 2023
Available online 31 October 2023

tRNA synthetase, reverse transcriptase, carboxypeptidase and superoxide dismutase (Twining and Baines, 2013; Ye et al., 2022). The enzyme carbonic anhydrase catalyses the reversible hydration of bicarbonate to carbon dioxide; hence, it plays an important role in inorganic carbon acquisition by phytoplankton (Morel et al., 1994). In 1994, Morel et al. (1994) introduced the 'zinc hypothesis', which is analogous to the 'iron hypothesis' of John Martin, whereby zinc, like iron, is hypothesised to 'limit oceanic production and influence the global carbon cycle' (Morel et al., 1994). In the Southern Ocean, there has been no evidence of zinc limitation. The dissolved zinc concentration in most parts of the Southern Ocean is more than the concentration of zinc-binding ligands due to the upwelling of zinc and nutrient-rich deep waters (Baars and Croot, 2011; Ellwood, 2004). Indeed, the surface dissolved zinc concentrations are highest in the Antarctic Zone at ~4 nM, decreasing to below 0.5 nM in the Subantarctic Zone (e.g. Ellwood et al., 2020a; Sieber et al., 2020; Zhao et al., 2014). Consequently, the concentration of bioavailable zinc is more than enough to support phytoplankton growth. It is only in the northern reaches of the Subantarctic Zone where ligand concentrations exceed that of dissolved zinc, thus reducing zinc bioavailability (Baars and Croot, 2011; Ellwood, 2004; Sinoir et al., 2016).

Dissolved zinc isotopes have proven to be an insightful tool for tracing the processes involved in the cycling of zinc in the Southern Ocean and beyond (e.g. Conway and John, 2014; Ellwood et al., 2020a; Sieber et al., 2020; Sieber et al., 2023; Vance et al., 2019; Vance et al., 2017; Wang et al., 2019; Weber et al., 2018). The main oceanic processes that influence zinc isotope fractionation in the ocean appear to be biological uptake and regeneration (John et al., 2007; Köbberich and Vance, 2017, 2019; Samanta et al., 2018), ligand complexation (Marković et al., 2017; Sieber et al., 2023; Weber et al., 2018) and reversible scavenging (John and Conway, 2014; Sieber et al., 2023; Weber et al., 2018). In the Southern Ocean, variations in the isotope composition of dissolved zinc tend to be largest in the upper water column (range: 0 ‰ to +0.93‰) (Ellwood et al., 2020a; Samanta et al., 2017; Sieber et al., 2020; Wang et al., 2019; Zhao et al., 2014) while deeper waters (<500 m) are relatively homogenous around +0.45‰ (Ellwood et al., 2020a; Samanta et al., 2017; Sieber et al., 2020; Zhao et al., 2014). Sieber et al. (2020) and Ellwood et al. (2020a) noted that changes in iron bioavailability influences zinc isotope fractionation uptake by phytoplankton, although Sieber et al. (2020) noted increased fractionation upon iron fertilisation whereas Ellwood et al. (2020a) noted increased fractionation upon chronic iron limitation.

In culture studies, phytoplankton grown in replete zinc media typically have a lighter isotopic composition that those grown at low zinc concentrations, as the zinc uptake transitions from "passive" equilibrium control to an "active" kinetic control (John et al., 2007; Köbberich and Vance, 2017, 2019; Samanta et al., 2018). Zinc isotope fractionation tends to be greater when free Zn^{2+} concentrations are high. This transition from passive to active zinc control also influences the zinc content of cells, with the cellular Zn:P ratio recording this mechanistic change (John et al., 2007; Samanta et al., 2018; Sunda and Huntsman, 1992).

Measurements of dissolved zinc and silicic acid concentration versus depth reveal an almost congruent depletion of both elements in the surface ocean and enrichment with depth (Bruland et al., 1978). The similarity in the structure of the zinc and silicic acid profiles implies, at a superficial level, that zinc is cycled through the ocean in an analogous way to that of silicic acid. However, the zinc content of diatom frustule silica is low at around 3% (Ellwood and Hunter, 2000a).

Recent modelling efforts have resulted in two hypotheses for the coupling of zinc and silicic acid. The first idea is that this coupling is a result of biogeochemical modification of these Southern Ocean waters by diatoms combined with the physical circulation of waters through the Southern Ocean to propagate these patterns to low latitudes (de Souza et al., 2018; Vance et al., 2017). In tandem with this, reversible scavenging has also been modelled to explain the coupling of zinc and silicic acid, where surface-dissolved zinc is scavenged onto sinking detritus and is released at depth (Roshan et al., 2018; Sieber et al., 2023; Weber et al., 2018). While these modelling efforts are able to simulate the distributions of both zinc and silicic acid, they are primarily focused on the dissolved phase, with less attention paid to isotope fractionation processes associated with the particulate phase. This study aimed to culture Southern Ocean phytoplankton under conditions similar to those in this region to understand the pathways that might influence zinc uptake and isotope fractionation, especially when iron is growth-limiting. We complement these laboratory incubation experiments with a field experiment and water column measurements from three Southern Ocean sites.

2. Materials

2.1. Phytoplankton culturing

Two species of diatoms *Proboscia inermis* and *Chaetoceros flexuosus* were grown under controlled nutrient, light and temperature conditions with the only change variables being iron and zinc. *P. inermis* and *C. flexuosus* were isolated from 57°51.1′S; 139° 50.7′E in 2001 (Strzepek et al., 2011). Experimental cultures were grown at 3 ± 1 °C under a continuous irradiance of 60–70 μmol photons m^{-2} s^{-1}, which was optimal for these species. Irradiance was measured with a calibrated 4π quantum meter (model QSL-2101; Biospherical Instruments).

All vessels used for growing cultures were acid-cleaned and microwave sterilised. The cultures were acclimated in 28 mL polycarbonate tubes and maintained in the exponential phase of growth. At least two transfers (14–16 cell divisions) were undertaken before being transferred to 500 mL polycarbonate bottles. An artificial seawater medium (Aquil) was used for our trace metal manipulation experiments (Price et al., 1988). The base Aquil media was prepared using protocols detailed in Price et al. (1988) as modified by Strzepek et al. (2011). Synthetic seawater was prepared and gravity filtered through a Toyoperal AF-chelate-650 M (Tosoh Bioscience) ion-exchange resin to remove contaminating trace elements. The base media had an iron contamination concentration of 0.56 ± 0.02 nmol L^{-1}, which was accounted for in subsequent iron culture experiments. This media was sterilised through a 0.22 μm filter and microwaved. Background trace metals added were buffered with 10 μmol L^{-1} ethylene-diamine-tetra-acetic acid (EDTA) as a chelating agent. Final trace metal concentrations were for variable for $ZnSO_4$, 2.0 nmol L^{-1} for $CuSO_4$, 5 nmol L^{-1} for $CoCl_2$, 23 nmol L^{-1} for $MnCl_2$, 10 nmol L^{-1} for Na_2SeO_3 and 100 nmol L^{-1} for Na_2MoO_4. Final nutrient concentrations were 10 μmol L^{-1} for phosphate, 100 μmol L^{-1} for silicate, 300 μmol L^{-1} for nitrate, 0.55 μg L^{-1} for vitamin B12, 0.5 μg L^{-1} for Biotin and 100 μg L^{-1} for thiamin. The iron concentration of the media was manipulated using two different chelators: EDTA and desferrioxamine B mesylate (DFB). For the iron-replete media, hereafter referred to as pFe 19.4, iron was pre-complexed with EDTA at concentrations of 58 nmol L^{-1} (Fe) and 10 μmol L^{-1} (EDTA), respectively. For iron limiting experiments, the concentration of iron was kept constant at 4.0 nmol $L^{-1,}$ and an increasing concentration of desferrioxamine B mesylate (DFB) (4, 40, and 400 nmol L^{-1}) was added to the final Aquil media. Note that iron was pre-complexed to DFB prior to addition to the Aquil media.

Final free metal iron concentrations (−log free-metal ion concentration = pMetal) for the media were calculated using Visual MINTEQ version 3.1 (https://vminteq.lwr.kth.se/). pMetal values were as follows: pCu = 14.1, pCo = 11.5, pMn = 8.2 and pZn = 9.7 (Zn^{2+} = 190 pM), 10.7 (Zn^{2+} = 24 pM), 10.9 (Zn^{2+} = 12 pM), 11.8 (Zn^{2+} = 1.6 pM), and 12.2 (Zn^{2+} = 0.6 pM) for total zinc additions ranging from 0.3 to 100 nM. Inorganic iron (Fe') concentrations for the p19.4 media were calculated using methods described by Strzepek et al. (2011) for media at 3 °C, under irradiance of 70 μmol quanta m^{-2} s^{-1} and at a pH of 8.2. Unlike the iron-EDTA complex, the iron-DFB complex is not photosensitive, and hence iron speciation is not affected by light (Lis et al., 2015; Sunda and Huntsman, 2003). The Fe' for the iron limiting media was

calculated according to the equation [Fe'] = [FeDFB] / [L'] × $K^{cond}_{Fe'L}$; where $K^{cond}_{Fe'L} = 10^{11.8}$ (Maldonado et al., 2005).

Growth rate data were collected from cultures acclimated to experimental zinc and iron treatments for a minimum of three transfers. Growth rate measurements were made on cells maintained in the exponential phase of growth, which generally lasted between 10 and 20 days. Growth rates were determined from in vivo chlorophyll *a* fluorescence using a Turner Designs model 10-AU fluorometer and measured once every alternate day. Cultures were dark acclimated for approximately 30 min prior to each fluorescence measurement. The specific growth rate per day (μ) was then calculated by determining the slope of ln(fluorescence) versus cumulative time during the exponential growth phase.

2.2. Elemental and isotope analysis

Acid-cleaned polycarbonate filters (2 μm) were used to collect cell material for silica and trace metal analysis. For silica analysis, between 50 and 70 g of culture water was filtered for analysis. For metal and phosphorous analysis, approximately 350 g of culture water was filtered for analysis under a low vacuum. Biogenic silica samples were stored in 50 mL acid-cleaned falcon tubes at -20 °C, and trace metal samples were stored in 5 mL acid-cleaned Teflon vials (Savillex, USA) at 25 °C. The organic and inorganic (frustule) fractions for trace metal analysis were separated by adding 5 mL of 7 mol L^{-1} Teflon-distilled nitric acid to each sample vial. Samples were mixed and left for 24 h, after which the filter within each vial was carefully rinsed with Milli-Q water and removed. The vials were then left to reflux for 12 h on a hotplate and then uncapped and taken to dryness. The samples were then redissolved in 5 mL in 2% HNO_3. After a suitable settling period, a 4 mL aliquot was removed from each vial for organic material analysis. The remaining 1 mL, containing diatom frustule remains, was transferred to a 15 mL centrifuge tube. Vials were then filled to 14 mL with 18.2 MΩ Milli-Q and shaken to ensure mixing. This solution was removed following centrifugation for 10 min at 5000 rpm. This Milli-Q rinsing process was repeated an additional two times. The zinc concentration of the final rinse solution was tested and found to be comparable to blank concentrations. The remaining frustule was then dissolved in 0.1 mL of 2.6 mol L^{-1} sodium hydroxide (Suprapur, Sigma Aldrich) for 24 h in acid-clean Teflon vials. After which, the volume was increased to 5 mL with Milli-Q. The sodium hydroxide solution had a background zinc level of 1.35 ± 0.11 ng zinc. A 0.5 mL aliquot of the digest was removed for silica analysis. The remainder of the inorganic fraction was then neutralised using 8 mol L^{-1} Teflon-distilled hydrochloric acid and then taken to dryness. The resultant residue was prepared for metal analysis.

Biogenic silica concentrations were determined colourimetrically following dilution to 10 mL (Strickland and Parsons, 1972). Working standards were prepared by diluting a commercially available 1000 mg Si L^{-1} standard (TraceCert, Merck). The working concentration range was 0 to 20 μmol L^{-1}.

One mL aliquot from the organic material analysis fraction was removed for zinc and phosphorus content determination by High-Resolution Inductively Coupled Plasma Mass Spectrometry (Element XR, TheromScientific). Five calibration standards were made from certified trace metal, and phosphorus concentration standards (TraceCert, Merck) with zinc to phosphorus of ratios of 2:20, 5:50, 10:100, 50:500 and 100:1000 (ng mL^{-1}: ng mL^{-1}); and were measured at the beginning of the session. A blank measurement was done on 2% nitric acid. Instrument drift was monitored by running standard every tenth sample. The zinc:phosphorous error bars reported are for each treatment and represent the standard deviation of three culture (biological) replicates i.e. each biological replicate represents an independently grown culture that then is fully processed for elemental and isotope analysis.

Zinc concentration for inorganic fractions was determined by High-Resolution Inductively Coupled Plasma Mass Spectrometry (Element XR, ThermoScientific) using a similar procedure for measuring the organic fraction. The zinc:silicon results were for the inorganic frustule remains, and error bars reported are for each treatment and represent the standard deviation of three biological replicates.

The remaining 3 mL of the organic material analysis fraction was taken to dryness and then dissolved in 6 mol L^{-1} hydrochloric acid in preparation for anion exchange column chemistry. Zinc and iron were isolated from the organic and inorganic fractions by using the AG MP-1 anion exchange resin following zinc double spike (DS) addition (Ellwood et al., 2020a; Samanta et al., 2018).

Zinc isotope measurements were made using the Multicollector-ICPMS (Thermo Scientific Neptune Plus) along with a desolvating sample introduction system (Apex IR, Elemental Scientific Inc.) with an uptake rate of ~50 μL per minute. A standard nickel sampler cone and a nickel X-skimmer cone were used to enhance instrument sensitivity. The instrument was operated in medium resolution mode, and samples were measured in groups of two, bracketed with a standard-DS mixture. A 2% (*v*/v) nitric acid wash was introduced between sample and standards, and blank measurements were made on 2% nitric acid solution before every sample and standard measurements. All measurements were made as 1 block of 45 cycles with a 4-s integration time. At the start of each measurement session, the instrument was tuned for intensities on mass ^{62}Ni, ^{63}Cu, ^{65}Cu, ^{64}Zn, ^{66}Zn, ^{67}Zn and ^{68}Zn.

The zinc isotopic composition was expressed in delta notation following the equation:

$$\delta^{66}Zn = \left(\frac{{}^{66}Zn / {}^{64}Zn_{sample}}{{}^{66}Zn / {}^{64}Zn_{standard}} - 1 \right) \times 1000 \quad (1)$$

All zinc isotope measurements in the study were measured relative to the standard reference material IRMM-3702. Note field seawater isotope values were corrected to the JMC Lyon standard ($\delta^{66}Zn_{Lyon}$) by adding 0.3 ‰ (Archer et al., 2017). Multiple measurements of an in-house check standard (Koch) and the AA-ETH standard over multiple isotope sessions between 2017 and 2022 produced values of −0.72 ± 0.09 ‰ (n = 86, ± 2× standard deviation (SD)) and 0.00 ± 0.08 ‰ (n = 115, ± 2SD), respectively. The value we obtained for the AA-ETH standard is indistinguishable from the published value of 0.00 ± 0.02 ‰ (Archer et al., 2017). The isotopic composition of zinc added to Aquil media was 0.06 ± 0.01 ‰ (n = 3, ± 2SD) and well with the error representing two standard deviations of three culture (biological) replicates and averaged ±0.22 ‰ (n = 28, ± 2SD). These errors associated with triplicate cultures were larger than the sample processing and instrumental error of ±0.06 ‰ (n = 28, ± 2SD).

2.3. Field incubation experiment

One deck-board incubation experiment involving various spike combinations of zinc, iron and silicate, was conducted at the Southern Ocean Time Series site (SOTS)(47°S; 142°E) in mid-March 2019. This site is located in subantarctic waters and is characterised by low zinc and silicic acid conditions with variable productivity depending on iron supply (Boyd et al., 2001; Ellwood et al., 2020a; Eriksen et al., 2018; Sedwick et al., 1999). A 50 L carboy was rinsed and then filled to surface seawater using a trace metal (TM) clean towed 'Fish' system (Ellwood, 2004). The 1 L polycarbonate bottles were then rinsed 3 times with unfiltered TM Fish water and then filled with 1 L of water from the 50 L carboy. Ten treatments were undertaken in triplicate with varying concentrations of zinc, iron and silicate (Table 1). Prior to its addition, iron was pre-complexed to EDTA in a 1:1 ratio to prevent its precipitation upon addition to seawater. The bottles were incubated in a flow-through incubator at ambient surface seawater temperature (~11 °C). Flow-through incubators were partial shading using green shade cloth, which reduced light levels by about 85%, simulating ambient conditions of the mixed layer. Treatments were sampled on days 4, 6, 8 and 10 for F_v/fm and F_0 (fluorescence) to generate a growth curve from the natural log of the initial fluorescence measurement versus time. Community

Table 1
Summary of dissolved trace metal and nutrient additions for each incubation treatment that were undertaken in triplicate.

Treatment ID	Fe (nM)	$Si(OH)_4$ (μM)	Zn (nM)	$\delta^{66}Zn_{Lyon}$(‰)
Control[⁋]	0.18 ± 0.07	1.6	0.58 ± 0.15	−0.23 ± 0.06
Si	0.18	102	0.58	−0.23 ± 0.06
Zn	0.18	1.6	4.5	0.31 ± 0.08[#]
LFe	0.87	1.6	0.58	−0.23 ± 0.06
LFeSi	0.87	102	0.58	−0.23 ± 0.08
LFeSiZn	0.87	102	4.5	0.31 ± 0.08[#]
HFe	5.8	1.6	0.58	−0.23 ± 0.06
HFeSi	5.8	102	0.58	−0.23 ± 0.06
HFeZn	5.8	1.6	4.5	0.31 ± 0.08[#]
HFeSiZn	5.8	102	4.5	0.31 ± 0.08[#]

[⁋] Initial trace metal and isotope composition of the water used at the start of the experiment. This is based on multiple (n = 4) measurements of the trace metal clean "fish" water used for the experiment.

[#] The isotopic composition of seawater following the zinc addition. $\delta^{66}Zn$ values have been corrected to the JMC Lyon standard by adding 0.3 ‰ (Archer et al., 2017).

growth rates were calculated by regressing sample fluorescence versus time. At the end of the incubation, 900 mL of sample was collected on acid cleaned 47 mm 0.2 μm polycarbonate membrane filter (Whatman Nuclepore), under a low vacuum. Each sample was washed twice with 0.45 μm filtered TM Fish water and stored at -20 °C until analysis. Trace metal, silica and phosphorous were determined as outlined in the elemental and isotope analysis section. For particulate organic carbon and nitrogen analysis (POC/PON), 60 mL of sample was syringe filtered through a precombusted 13 mm GF/A filter and rinsed with a small volume of filtered TM Fish water and stored at −80 °C until analysis. POC and PON were determined using standard procedures (Andrew et al., 2022).

2.4. Dissolved and particulate zinc profiles

Samples were collected for dissolved and particulate zinc concentrations and isotope analysis at three stations in the Southern Ocean during the Southern Ocean Large Areal Carbon Export (SOLACE) voyage over December 2020–January 2021 (https://solace2020.net/). The stations were located at the SOTS, Southern Site 1 (SS1)(55°50′S 139°00′E) and Southern Site 2 (SS2)(58°00′S 141°30′E) (Fig. S1). All three sites were characterised by high phytoplankton numbers with a prevalence of diatoms (Boyd et al., 2023; Latour et al., 2022).

Dissolved and particulate sample collection protocols were similar to those outlined by Ellwood et al., 2020a and Ellwood et al., 2020b. Briefly, filtered samples were collected for trace metal, and zinc isotope determination using acid-cleaned, Teflon-coated, externally-sprung, 12-l Niskin bottles attached to an autonomous rosette (SeaBird) equipped with an SBE 911plus CTD unit (SeaBird). Particulate trace metal samples were collected in situ onto acid-leached 0.2-μm PVDF (142 mm diameter) filters (Sterlitech) using six large-volume dual-head pumps (McLane Research Laboratories) deployed at various water depths. The pumping volume range from 30 L in the surface water to over 300 L in the deep. For several profiles, one pump depth was used as a blank check whereby only 4-5 L of water was pumped through the filter.

Dissolved and particulate zinc concentration and isotope determination followed the protocols outlined by Ellwood et al. (2020a) and above. Blanks for dissolved and particulate zinc were 3 ± 2 ng and 20 ± 2 ng, respectively. The $\delta^{66}Zn_{Lyon}$ composition of the particulate blank was 0.11 ± 0.10 ‰ (±2 SD). The main Zn contributor to the particulate blank, based on water column deployment of pumps, came from the PVDF filters (84%), with the remaining (16%) coming from sample handling and processing reagents. The particulate blank contribution to most samples was <10% of the total zinc concentration, except for some SOTS samples where particulate concentrations were low. All particulate zinc isotope sample values were blank-corrected with a median correction of 0.02 ‰ (n = 37). Only four samples had a correction of >0.1 ‰. As an accuarcy check, we also measured the zinc isotope composition of BCR414 using our particulate digestion protocol and obtained a value of 0.33 ± 0.07 ‰, which is consistent with the values of 0.32 ‰ and 0.29 ‰ obtained by Druce et al. (2020) and Jeong et al. (2021), respectively. The reproducibility for multiple analyses of a large volume deep-water and shallow-water dissolved samples was excellent, with average concentrations of 5.14 ± 0.09 nmol kg^{-1} (n = 4, 2×SD) and 0.07 ± 0.06 nmol kg^{-1} (n = 2, 2×SD), respectively, and average isotope value of 0.37 ± 0.08 ‰ (n = 4, 2x SD) and 0.10 ± 0.02 ‰ (n = 2, 2xSD), respectively.

3. Results

3.1. Cellular growth rate

The specific growth rates for cells grown under iron-replete (Fe' = 3369 pmol L^{-1}) across a range of conditions at a Zn^{2+} concentration ranged between 0.33 d^{-1} and 0.51 d^{-1} for *P. inermis* and 0.11 d^{-1} and 0.42 d^{-1} *C. flexuous* (Fig. 1A, D and Table 2). Below a Zn^{2+} concentration of 12 pmol L^{-1}, *P. inermis* would not grow, indicating a high requirement for zinc. Conversely, *C. flexuous* grew even at the lowest Zn^{2+} concentration of 0.6 pmol L^{-1}. These growth rates obtained at the two highest Zn^{2+} concentrations are comparable to that obtained in previous culture studies involving these species under similar iron-replete conditions (Andrew et al., 2019; Strzepek et al., 2011). The optimum growth rate for both species was obtained for iron replete at a Zn^{2+} concentration of around 24 pmol L^{-1}.

3.2. Effect of iron on cellular the Zn:P ratio

Cellular Zn:P ratios for *P. inermis* and *C. flexuosus* declined as the Zn^{2+} concentration of the medium was reduced (Fig. 1B,E; Table 2). This occurred for all iron treatments when Zn^{2+} was varied. Interestingly, for cells grown at a fixed Zn^{2+} concentration, the cellular Zn:P ratio increased when the iron concentration was reduced. For example, for *P. inermis* cells grown at a Zn^{2+} concentration of 190 pM, the cellular Zn:P ratio increased 10-fold from 8.9 mmol:mol to 87.9 mmol:mol as Fe' was lowered from 3369 nM to 0.02 nM. A similar increase in the cellular Zn:P ratio was observed for *C. flexuosus* grown at a similar Zn^{2+} concentration (Fig. 1). At the lower Zn^{2+} concentrations, the increase in the cellular Zn:P ratio was more muted upon iron limitation. For example, for *C. flexuosus* the Zn:P ratio increased approximately 1.2-fold at Zn^{2+} concentrations of 12 pM and 1.6 pM (Fig. 1; Table 2).

The cellular Zn:P ratios measured here are slightly high than that determined for temperate phytoplankton grown across a similar range of Zn^{2+} values (Fig. 2) (e.g. Ellwood and Hunter, 2000a; John et al., 2007; Sunda and Huntsman, 1992), but consistent with values estimated for from the work of Koch and Trimborn (2019) for the polar species *C. simplex*. Our cellular Zn:*P* values are similar to the range (2.14 mmol:mol to 17 mmol:mol) obtained for Southern Ocean phytoplankton collected from the field, although this range includes iron-replete and iron-limited phytoplankton. The cellular Zn:P ratios for *P. inermis* and *C. flexuosus* are also within the range measured for non-descript particulates collected from the Southern Ocean (Fig. 2B)(e.g. Collier and Edmond, 1984; Cullen et al., 2003; Ellwood et al., 2020a; Twining and Baines, 2013).

The specific zinc uptake rate for these *P. inermis* and *C. flexuosus* showed a similar pattern to Zn:P ratios versus Zn^{2+} concentration (Fig. 2). Specific uptake rates for *P. antarctica* and *P. inermis* fall within the bounds of the sigmodal relationship for zinc uptake obtained for the coccolithophore *E. huxleyi* and diatom *T. oceanica* (Fig. 2A) (Samanta et al., 2018; Sunda and Huntsman, 1992).

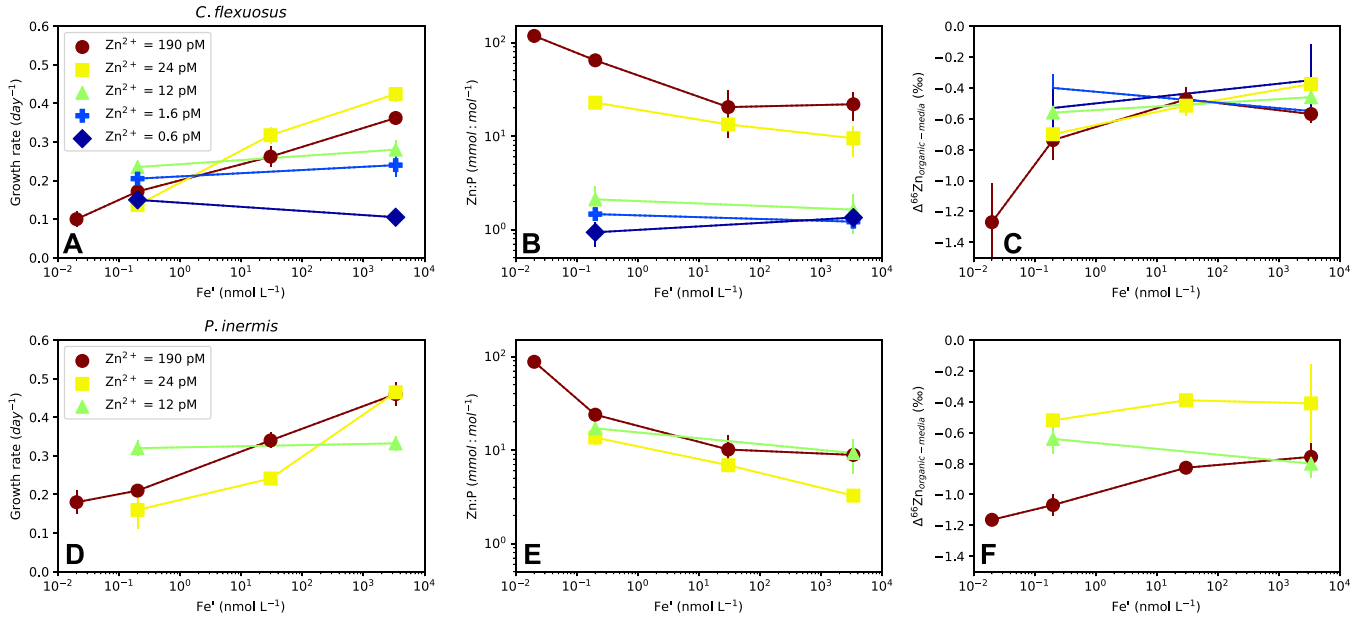

Fig. 1. Variation in specific growth rate (A., D.), zinc normalised to phosphorous content (B., E.), and zinc isotope composition (C., F.) for *C. flexuous* and *P. inermis* grown across a range of Fe' concentrations and a range of free Zn^{2+} concentrations (Table 2).

Table 2
Growth rate, Zn:P ratio and zinc isotope composition of organic and frustule matter and the Zn:Si ratio of *P. inermis* (Pi) and *C. flexuosus* (Cf) grown across a range of dissolved inorganic Fe and Zn^{2+} concentrations. The values represent mean values for triplicate biological replicates. Errors are two standard deviations for isotope values from biological replicates and one standard deviation for other values from biological replicates.

Species	Zn^{2+} (pmol L^{-1})	Fe' (pmol L^{-1})	Growth rate (d^{-1})		Zn:P (mmol:mol)		$\Delta^{66}Zn_{organic\text{-}media}$ (‰)		$\Delta^{66}Zn_{frustule\text{-}media}$ (‰)		Zn:Si (μmol:mol)	
Cf	190	3369	0.36	±0.02	22	±7	−0.57	±0.06	−1.05	±0.34	188	±168
Cf	190	30.1	0.26	±0.03	20	±11	−0.47	±0.08	−1.03	±0.09	352	±210
Cf	190	0.2	0.17	±0.01	65	±4	−0.74	±0.13	−0.90	±0.19	590	±592
Cf	190	0.02	0.10	±0.02	118	±18	−1.27	±0.26	−0.98	±0.17	412	±364
Cf	24	3369	0.42	±0.02	10	±3	−0.38	±0.21	−0.80	±0.19	23	±4
Cf	24	30.1	0.32	±0.02	13	±1	−0.52	±0.06	−0.50	±0.08	33	±14
Cf	24	0.2	0.14	±0.02	23	±1	−0.70	±0.07	−0.49	±0.21	26	±8
Cf	12	3369	0.28	±0.02	1.6	±0.7	−0.46	±0.09				
Cf	12	0.2	0.24	±0.02	2.1	±0.8	−0.56	±0.02				
Cf	1.6	3369	0.24	±0.03	1.2	±0.1	−0.55	±0.05				
Cf	1.6	0.2	0.21	±0.02	1.5	±0.2	−0.40	±0.09				
Cf	0.6	3369	0.11	±0.01	1.3	±0.2	−0.35	±0.23				
Cf	0.6	0.2	0.15	±0.02	0.9	±0.3	−0.53	±0.13				
Pi	190	3369	0.46	±0.03	8.9	±1.7	−0.76	±0.12	−1.02	±0.39	90	±23
Pi	190	30.1	0.34	±0.02	10	±4	−0.83	±0.02	−0.83		100	±6
Pi	190	0.2	0.21	±0.01	24	±4	−1.07	±0.07	−0.71	±0.19	263	±41
Pi	190	0.02	0.18	±0.03	88	±2	−1.16	±0.04	−0.56	±0.27	239	±32
Pi	24	3369	0.46	±0.02	3.3	±0.4	−0.41	±0.25	−0.32	±0.06	20	±18
Pi	24	30.1	0.24	±0.01	6.9	±0.6	−0.39	±0.04	−0.40	±0.06	38	±17
Pi	24	0.2	0.16	±0.05	14	±2	−0.52	±0.04	−0.37	±0.10	56	±11
Pi	12	3369	0.33	±0.02	9	±4	−0.80	±0.09				
Pi	12	0.2	0.32	±0.02	17	±2	−0.64	±0.10				

3.3. Stationary phase experiments

For a few experiments, cells were allowed to reach the stationary phase of growth (between 12 and 100 days after experiment initiation) at two Zn^{2+} concentrations; 23 and 190 pM. For these cultures, the cellular Zn:P values were lower than cells harvested in the exponential growth phase when cultured across a range of Fe′ concentrations (Fig. 3), indicating a loss of zinc from organic material.

3.4. Effect of iron on the frustule Zn:Si ratio

Frustule Zn:Si ratio data were obtained for *P. inermis* and *C. flexuosus* grown at the two highest Zn^{2+} concentrations, 190 pM and 24 pM – at lower Zn^{2+} concentrations, we were not able to obtain enough zinc to make reliable Zn:Si measurements. Zn:Si ratios ranged between 20 and 590 μmol:mol and scaled with changes in Zn^{2+} and Fe' concentrations (Fig. 4A,C). Zn:Si ratios declined when the Zn^{2+} concentration was lowered from 190 pM to 24 pM; however, frustule Zn:Si ratios tended to increase with increasing iron limitation Figure 4. For example, the Zn:Si ratio for *P. inermis* grown at a Zn^{2+} concentration of 24 pM was 20 ± 18 μmol:mol at an Fe' concentration of 3369 nM and increased to 50 ± 11 μmol:mol when the Fe' concentration was lowered to 0.2 nM (Figure 4, Fig. 5 and Table 2).

The percentage of zinc with the frustule ranged between 5% and 18% for *P. inermis* and *C. flexuosus* (with 3 outliers removed >3 σ, $n = 39$) with no apparent trends in the data. The percentage value for

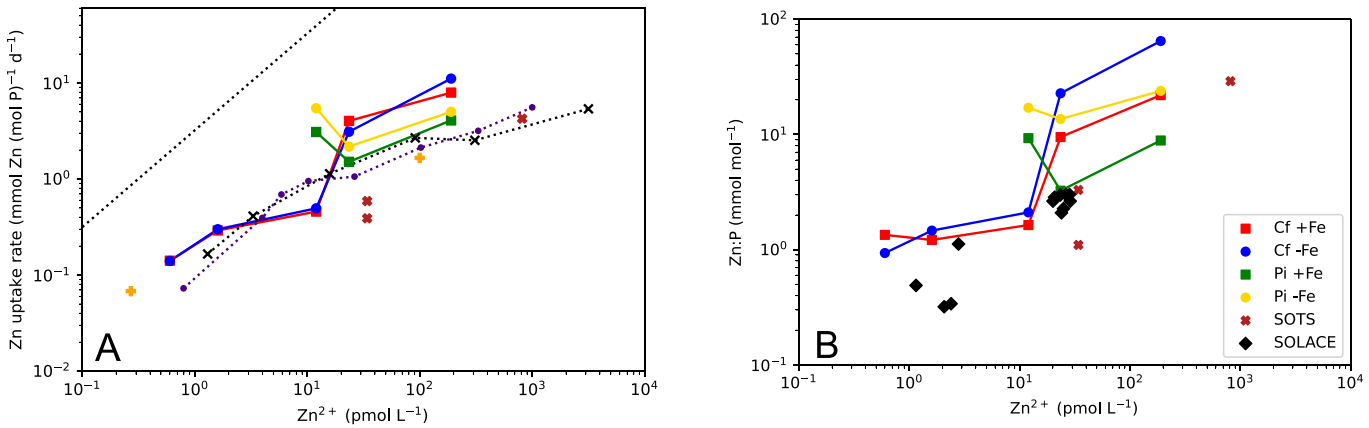

Fig. 2. A. Specific uptake rates for zinc normalised to phosphorus content for *C. flexuosus* and *P. inermis* and grown under iron-replete (Fe' = 3369 nM) and iron-limiting (Fe' = 0.2 nM) conditions. Also presented are specific uptake rates for *E. huxleyi*, *T. oceanica* and *C. simplex* taken from Samanta et al. (2018), Sunda and Huntsman (1992) and Koch and Trimborn (2019), respectively. The Sunda and Huntsman (1992) and Koch and Trimborn (2019) datasets were converted from Zn:C to Zn:P by converting carbon to phosphorus using a Redfield stoichiometry of 106:1. SOTS 2019 incubation data for the control and + Zn only treatments. The free Zn^{2+} concentrations for the SOTS 2019 incubation experiment were calculated from the dissolved zinc concentration, assuming an organic ligand concentration of 2 nM, a conditional stability constant (K'_{ZnL}) equal to 10^{10} and an inorganic side-reaction coefficient between free Zn^{2+} and inorganic Zn' complexes of 2.1. The dashed line represents the maximum uptake rate of Zn under diffusion control for Southern Ocean conditions. B. Zinc normalised to phosphorus for laboratory cultures, the incubation (as in A) and upper water column (<100 m) field samples collected at the SOTS site and two polar sites, SS1 and SS2. The free Zn^{2+} concentrations were calculated as detailed in A.

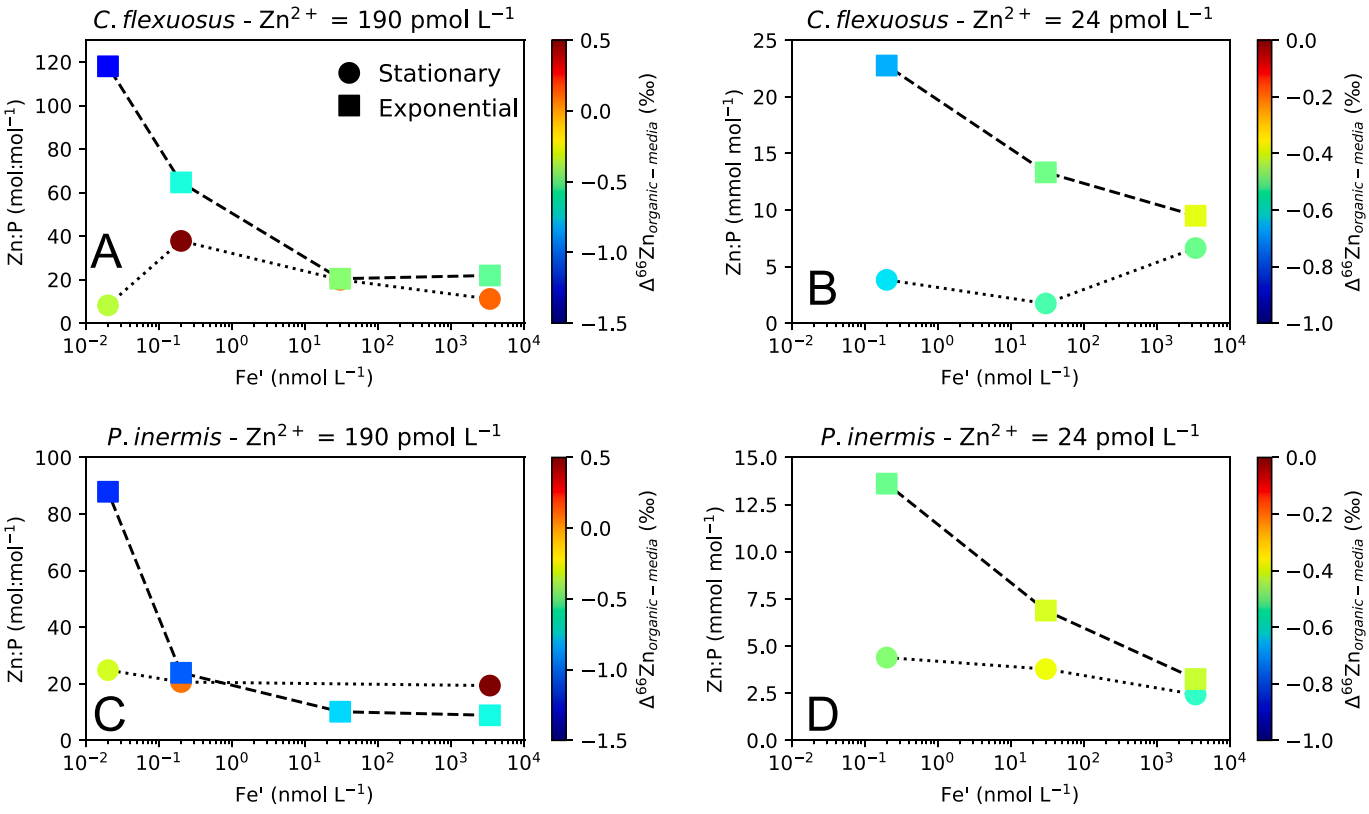

Fig. 3. Variations in the zinc normalised to phosphorus ratio and zinc isotope composition of organic matter for *C. flexuous* (A., B.) and *P. inermis* (C., D.) and grown across a range of Fe' concentrations, but at two fixed Zn^{2+} concentrations (24 pmol L^{-1} and 190 pmol L^{-1}). Cells were either harvested during the exponential phase of growth or once they were in the stationary phase of growth. Note the change in the isotope range for the colour bars between the two free Zn^{2+} concentrations.

C. flexuosus is likely to be slightly underestimated as a result of siliceous spine loss during frustule isolation.

3.5. Cellular zinc isotopes

The zinc isotope composition ($\Delta^{66}Zn_{cells-media}$) for the organic components of *C. flexuosus* and *P. inermis* was isotopically light relative to the culture media (Figs. 2 and 6). At higher free Zn^{2+} concentrations, isotope fractionation was greater than for cells grown at lower free Zn^{2+} concentrations (Fig. 6). Zinc isotope fractionation also varied depending on the Fe' concentration of the media, with isotopically light values obtained for cells grown at lower Fe' concentrations compared to cells

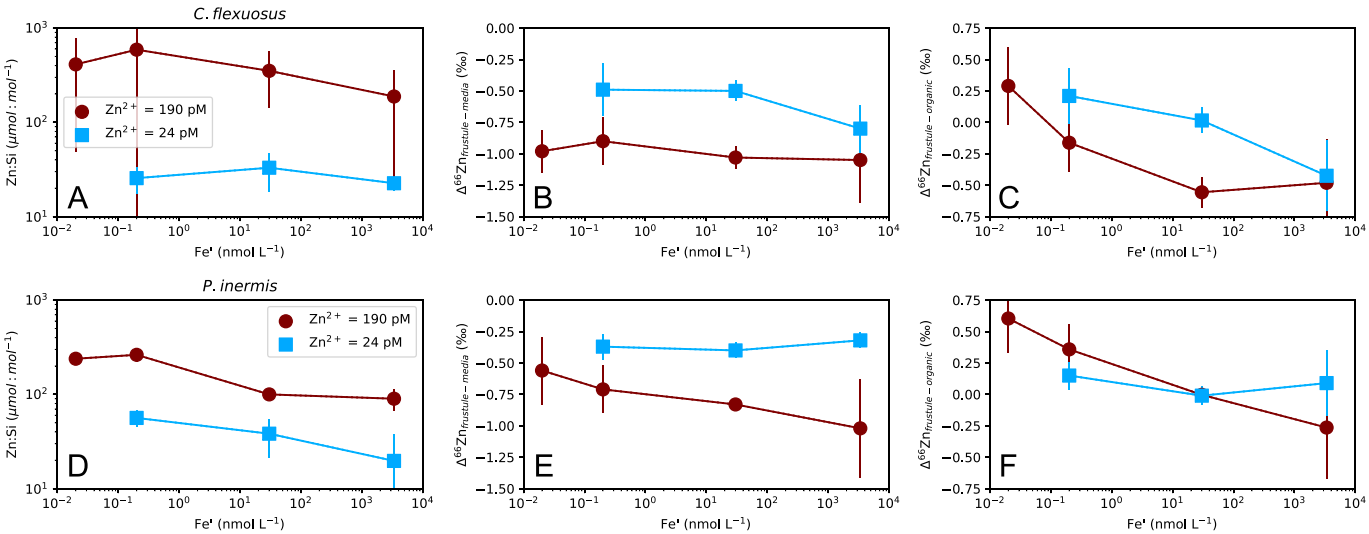

Fig. 4. Variation in the zinc normalised to silica content (A., D.), the zinc isotope composition of frustule material (B., E.) and the isotope difference between the isotope content of frustule material and organic material (C., F.) for *C. flexuous* and *P. inermis*.

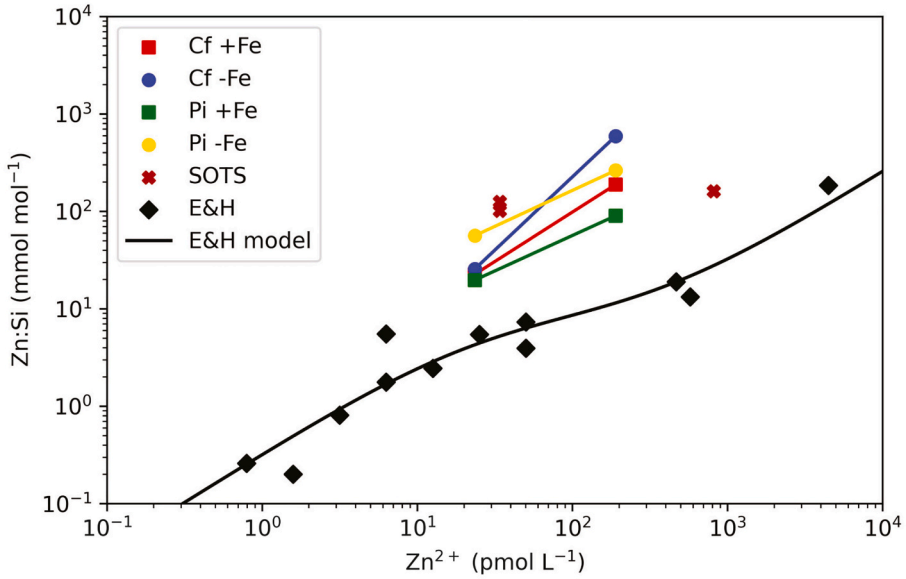

Fig. 5. Variations in the zinc normalised to silica content for *C. flexuous* and *P. inermis* frustules grown under iron-replete (Fe' = 3369 nM) and iron-limiting (Fe' = 0.2 nM) conditions and a field incubation undertaken at the SOTS site in 2019 (See Fig. 2 caption for details). The field incubation data are for the control and + Zn only treatments. Also presented are results for *T. pseudonana* (E&H 2000). Data were taken from Ellwood and Hunter (2000a).

grown at higher concentrations (Fig. 1C and F). For example, for iron-replete cultures of *C. flexuosus* and *P. inermis* cultured at a Zn^{2+} concentration of 190 pM, $\Delta^{66}Zn_{cells\text{-}media}$ values declined from -0.57 ± 0.06 and -0.76 ± 0.12 ‰, respectively, to values of -1.27 ± 0.26 ‰ and -1.16 ± 0.04 ‰, respectively at an Fe′ concentration of 0.02 pM. At lower Zn^{2+} concentrations, isotope fractionation was less pronounced but still trended to light values with an increasing degree of iron limitation (Fig. 4).

3.6. Frustule zinc isotopes

The zinc isotope composition for the frustule ($\Delta^{66}Zn_{furstule\text{-}media}$) components of *C. flexuosus* and *P. inermis* were isotopically light relative to the culture media when grown under iron-replete conditions (Fig. 4). Interestingly, upon iron limitation, $\Delta^{66}Zn_{furstule\text{-}media}$ trended to heavier values, which is the opposite of that observed for the organic fraction of *C. flexuosus* and *P. inermis* where values trended to lighter values upon iron limitation (cf Fig. 4B and E versus 1C and 1E). This was reflected in the isotope difference of the frustule zinc relative to organic zinc ($\Delta^{66}Zn_{furstule\text{-}organic}$), which trended to have positive values upon iron limitation (Fig. 4C and F).

3.7. Field incubations

For the incubation experiments, there was an increase in community growth rate for the treatments with added silica, added iron and combinations of two nutrients relative to the control (Fig. 7, Table 3). The main beneficiary of silica and iron addition was the large diatom community, with cell numbers visually increasing over that of the control. The addition of zinc on its own did not significantly stimulate growth; however, its addition and in combination with silica and iron (HZn, HFeZn, LFeZnSi and HFeZnSi) led to higher cellular Zn:P ratios (Fig. 7).

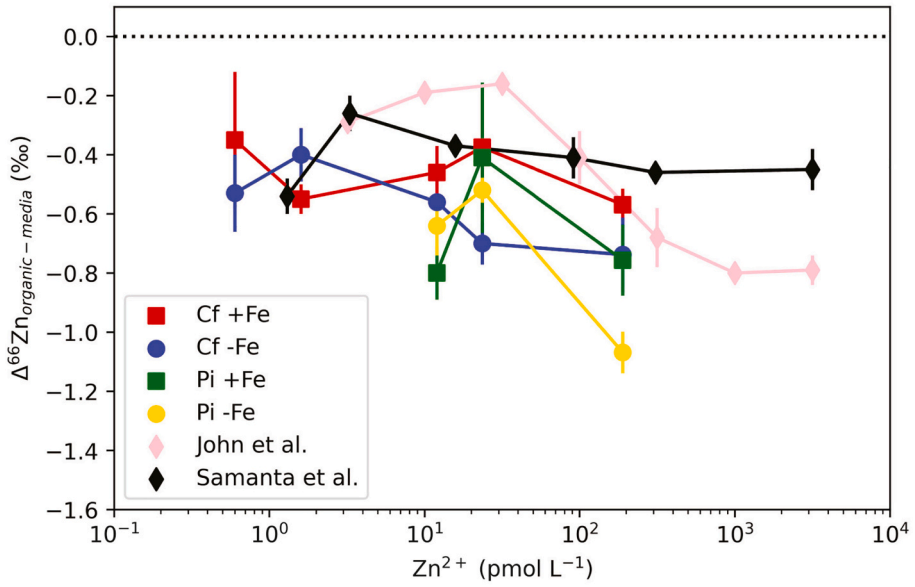

Fig. 6. Comparison of zinc isotope composition for *C. flexuous* and *P. inermis* grown across a range of Zn^{2+} concentrations, under iron-replete (Fe' = 3369 nM) and iron-limiting (Fe' = 0.2 nM) to values obtained by Samanta et al. (2018) and John et al. (2007) for *E. huxleyi* and *T. oceanica*, respectively.

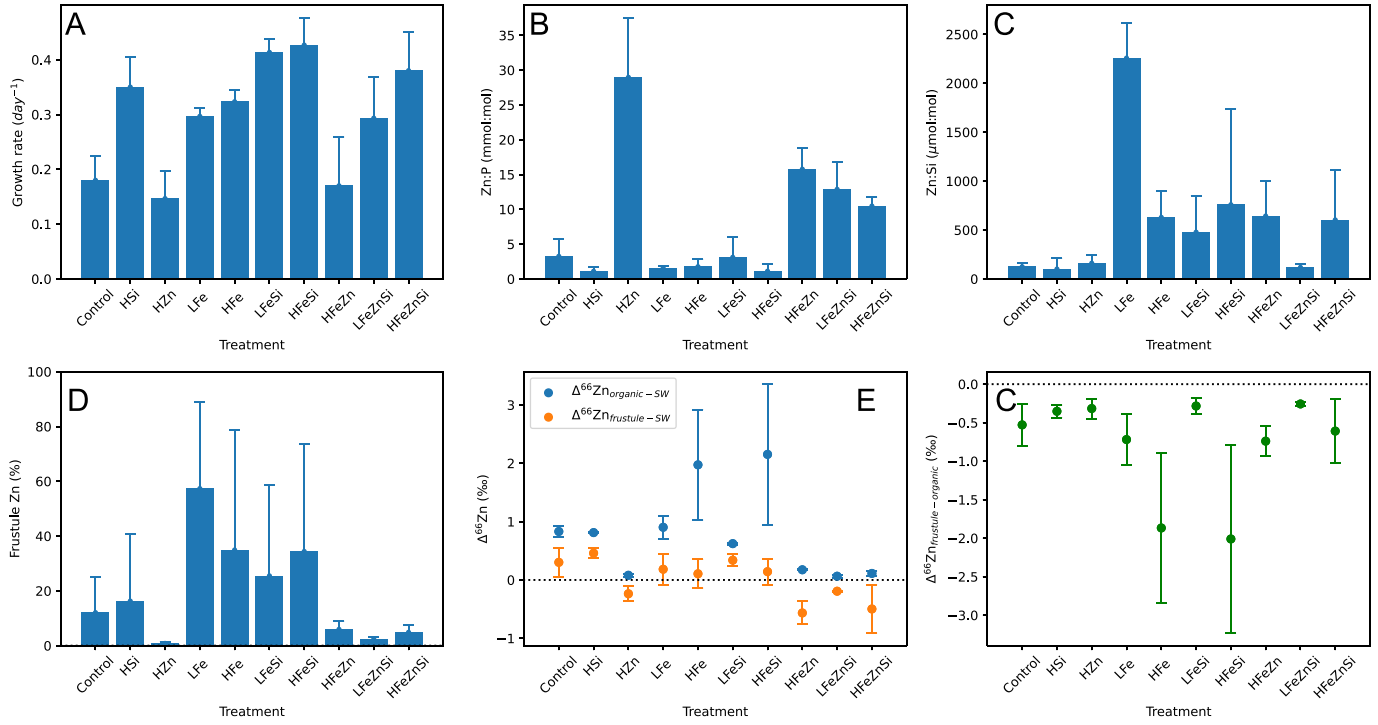

Fig. 7. Variations in plankton community from field incubations A. growth rate, B. zinc normalised to phosphorus content, C. zinc normalised to silica content for biogenic silica material, D. percentage of zinc within the biogenic silica, E. the zinc isotope composition of frustule material and organic material relative to initial seawater (SW) conditions (Table 1) and F. and the isotope difference between isotope content of frustule material and organic material. Error bars represent one standard deviation for three biological replicates (Table 3).

Zn:Si ratios for the natural community were enhanced upon the addition of iron from a control value of 125 ± 41 μmol:mol to values that ranged between 118 and 2257 μmol:mol for the added iron treatments (Fig. 7).

For all incubation treatments, the zinc isotope composition of organic material was isotopically heavier than the biogenic silica components of the community (Fig. 7). For the control, HSi, LFe, LFeSi treatments, the zinc isotope composition for the organic and biogenic silica components were significantly heavier than the incubation water. For the other treatments, the zinc isotope composition of biogenic silica material was either close to the seawater value or lighter than the seawater composition. This was readily apparent for the HFeZn and HFeZnSi treatments with $\Delta^{66}Zn_{furstule\text{-}seawater}$ values of −0.57 ± 0.20 and − 0.50 ± 0.42 ‰, respectively. In contrast, the zinc isotope composition of the organic components $\Delta^{66}Zn_{organic\text{-}seawater}$ for the HFe and the HFeSi treatments was heavy, with values of 1.97 ± 0.95 and 2.15 ± 1.20 ‰, respectively. While these errors are large, they represent variability between biological replicates, with the analytical precision of individual $\delta^{66}Zn$ measurements, typically below 0.1 ‰.

Table 3
Field incubation growth rate, particulate zinc concentrations for organic and frustule components, zinc isotope composition of organic and frustule components and zinc organic normalised to phosphorus and frustule zinc normalised to biogenic silica for each incubation treatment.

Treatment ID	Growth rate (d^{-1})		$pZn_{organic}$ (nmol L^{-1})		$\Delta^{66}Zn_{organic\text{-}sw}$ (‰)		$pZn_{frustule}$ (nmol L^{-1})		$\Delta^{66}Zn_{frustule\text{-}sw}$ (‰)		pZn:pP (mmol mol^{-1})		pZn:pSi (mmol mol^{-1})	
Control	0.18	±0.04	0.41	±0.22	0.83	±0.10	0.056	±0.031	0.30	±0.25	3.25	±2.52	125	±41
HSi	0.35	±0.06	0.34	±0.14	0.81	±0.00	0.067	±0.074	0.46	±0.08	1.11	±0.65	101	±108
HZn	0.15	±0.05	3.41	±0.72	0.08	±0.02	0.028	±0.017	−0.24	±0.13	29.0	±8.5	161	±81
LFe	0.30	±0.02	0.36	±0.07	0.90	±0.20	0.477	±0.172	0.18	±0.22	1.57	±0.36	2257	±362
HFe	0.32	±0.02	0.45	±0.24	1.97	±0.95	0.242	±0.173	0.11	±0.20	1.76	±1.04	629	±273
LFeSi	0.41	±0.03	1.21	±0.89	0.62	±0.01	0.413	±0.236	0.34	±0.10	3.11	±2.96	478	±374
HFeSi	0.43	±0.05	0.48	±0.37	2.15	±1.20	0.250	±0.091	0.14	±0.22	1.11	±1.01	759	±982
HFeZn	0.17	±0.09	2.50	±0.18	0.17	±0.01	0.158	±0.066	−0.57	±0.20	15.8	±3.1	643	±361
LFeZnSi	0.29	±0.08	4.26	±0.47	0.06	±0.02	0.105	±0.020	−0.19	±0.01	12.9	±3.9	118	±38
HFeZnSi	0.38	±0.07	3.46	±0.36	0.11	±0.04	0.177	±0.080	−0.50	±0.42	10.5	±1.3	603	±515

3.8. Field profiles

Profiles of dissolved and particulate zinc concentration within the upper 100 m increased in concentration with increasing latitude south, with the SOTS site having lower concentrations compared to the two polar sites, SS1 and SS2 (Fig. 8, S2, S3 and S4). This was also reflected in the Zn:P ratio for particulate material. The lithogenic zinc contribution to the Zn:P ratios was negligible for all samples (maximum = 2%, average = 0.4 ± 0.5%, $n = 39$) based on the using a Zn:Al ratio of 0.36 mmol:mol for the lithogenic endmember.

Profiles of zinc isotope composition for dissolved and particulate zinc were dynamic, with the zinc isotope composition of particulate zinc isotopically heavier than dissolved zinc for profiles collected from the SOTS site (Fig. 8). In contrast, particulate zinc was isotopically lighter than dissolved zinc for profiles collected at the two polar sites, SS1 and SS2.

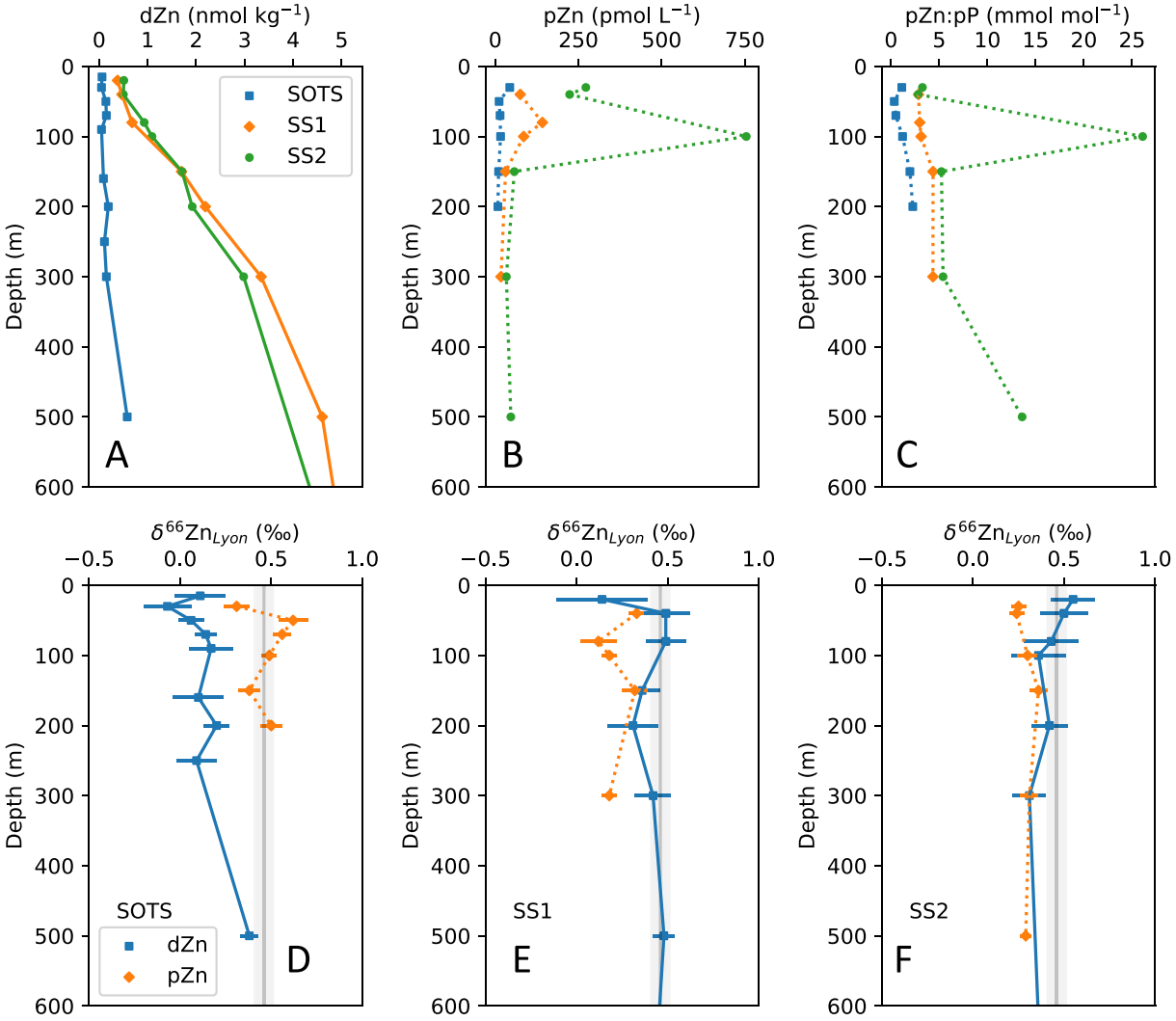

Fig. 8. Representative depth profiles of A. dissolved zinc (dZn) concentration; B. particulate (pZn) zinc (pZn) concentration and; C. particulate zinc to particulate phosphorus ratios for the SOTS, SS1 and SS2 sites. D. E. and F. representative zinc isotope profiles for dissolved and particulate zinc for the SOTS, SS1 and SS2 sites, respectively (Tables S2 and S3). The grey bars in the lower panels represent the deep ocean dissolved $\delta^{66}Zn$ average of +0.46 ± 0.05‰ (Sieber et al., 2023).

4. Discussion

4.1. Variations in cellular Zn:P and $\delta^{66}Zn$ ratios with iron limitation for cultured diatoms

Proboscia sp. and *Chaetoceros* sp. are members of the Southern Ocean diatom community that strongly influence the biogeochemical cycle of carbon through its uptake and eventual export into the deep ocean. Iron bioavailability strongly affects the growth of *P. inermis* and *C. flexuosus* (Fig. 1)(Andrew et al., 2019; Strzepek et al., 2011) and dramatically alters the elemental composition of their organic matter (Figs. 1B, E and 6B). The significant increase in the Zn:P ratio for the two phytoplankton species cultured in this study (Figs. 1 and 2) and the field incubations (Fig. 7) echo the trends seen by Cullen et al. (2003), whereby the Zn:P ratio of cells increased with declining iron bioavailability.

The increasing Zn:P ratios in response to declining iron bioavailability are likely coupled to physiological processes that enhance iron acquisition by cells. Cellular iron acquisition can be enhanced through the reduction of free and ligand-bound iron(III) to iron(II) at the cell surface (e.g. Coale et al., 2019; Shaked et al., 2005). Reduced iron can be transported of iron(II) into the cell is via the ZIP and NRAMP families of divalent metal transporters (Blaby-Haas and Merchant, 2017; Coale et al., 2019; Moreno et al., 2020) or reoxidised by ferridase and taken up (Coale et al., 2019). The upregulation of the divalent metal transporters under iron-limiting conditions is also likely to lead to increased zinc transport into cells and hence an increase in cellular Zn:P ratios with increasing iron limitation (Fig. 1B, D, Fig. 2B).

The enhanced removal of zinc relative to phosphorous for phytoplankton growing under iron-limiting conditions also needs to reconcile the zinc isotope composition of both sinking cells and remnant waters. The light zinc isotope composition measured in exponentially replicating phytoplankton (e.g. John et al., 2007; Köbberich and Vance, 2019; Samanta et al., 2018) has been attributed to either one or a combination of the following reasons: (i) lighter zinc being more readily bioavailable due to the preferential binding of heavier zinc by strong organic ligands present in seawater (or synthetic ligand EDTA in case of culture work) (Ban et al., 2002; Ding et al., 2010; Marković et al., 2017); (ii) the preferential retention of the heavier zinc isotopes at the zinc transport binding site(s) within the cell membrane (John et al., 2007); and (iii) the faster diffusion of lighter zinc through cellular ion channels resulting in lighter cellular zinc isotope composition (John et al., 2007; Köbberich and Vance, 2017; Samanta et al., 2018).

We observed variation in $\Delta^{66}Zn_{cells\text{-}media}$ values for exponential replicating phytoplankton cells, whereby cells grown at the high Zn^{2+} concentration, e.g. 190 pM, tended to be isotopically lighter than cells grown at the lower Zn^{2+} concentrations (Fig. 1C and F). This difference is likely associated with increased isotope fractionation when zinc is taken up via the 'low affinity' zinc uptake system, as has been reported for the diatom *T. oceanica* (CCMP 1005) and the coccolithophore *E. huxleyi* (CS-1016) (John et al., 2007; Samanta et al., 2018). The shift in dominance from the 'high affinity' diffusion-controlled pathway to a 'low affinity' pathway occurs at Zn^{2+} concentrations between 30 and 300 pM (John et al., 2007; Samanta et al., 2018; Sunda and Huntsman, 1992). The $\Delta^{66}Zn_{cells\text{-}media}$ values for *P. inermis* and *C. flexuosus* at Zn^{2+} concentration at 24 pM and below likely reflect zinc taken up via the punitive high-affinity zinc uptake pathway. Under equilibrium conditions, the $\delta^{66}Zn$ composition of the 'free' Zn^{2+} ions in the media is between −0.16 and − 0.33 ‰ lighter than zinc bound to EDTA (Ban et al., 2002; Ding et al., 2010; Marković et al., 2017), thus $\Delta^{66}Zn_{cells\text{-}media}$ values for *P. inermis* and *C. flexuosus* appear to reflect the $\delta^{66}Zn$ composition of 'free' Zn^{2+} ion pool in solution (Fig. 1D, F).

The role of DFB on zinc isotope fractionation in the incubation experiments also needs to be considered. The free metal ion concentrations for zinc, copper, manganese and cobalt in this study were maintained by complexation with EDTA, except for the iron-limited treatments where iron was mainly complexed to DFB. Quantum mechanical calculations suggest that heavier isotopes tend to form stronger bonds with ligands than their light isotope counterparts (Criss, 1999); however, there is limited knowledge of zinc isotope fractionation associated with zinc-DFB complexation. It has been suggested that phytoplankton may be able to take up zinc directly from the zinc-DFB complex via the formation of ternary complexes with zinc uptake ligands (Xu et al., 2012). However, the concentrations of DFB used in this study were at least 500 times less than the concentration of EDTA used, and the estimated stability constant for the zinc-DFB complex (logK = 9.55–10.36) is much lower than that of the zinc-EDTA complex (logK = 16.5) (Hernlem et al., 1996). Thus, we assumed that the isotopic composition of bioavailable zinc in the media would be the same at fixed concentrations of total zinc and EDTA in the presence of DFB. That said, we did notice that $\Delta^{66}Zn_{cells\text{-}media}$ tend to have more negative valves for iron-limited cells when expression of the divalent metal transporter is expected to be higher (Fig. 1C, F). Note the trends that we observe for *P. inermis* and *C. flexuosus* were different to Köbberich and Vance (2017), who observed the uptake of heavy zinc isotopes occurs under iron-limiting conditions. The change in zinc isotope fractionation we observe with an increasing degree of iron limitation is likely associated with upregulation of the divalent metal transport and not associated with isotope partitioning between zinc-DFB complex and seawater.

Coupled with the increase in Zn:P ratios upon iron limitation, an increase in the diatom frustule Zn:Si ratio for *P. inermis* and *C. flexuosus* was noted. These Zn:Si values are higher than determined for temperate phytoplankton grown across a similar range of Zn^{2+} values under iron-replete conditions (Fig. 5)(Ellwood and Hunter, 2000a) and Southern Ocean sedimentary values, which range between 1 and 14 μmol:mol (Andersen et al., 2011; Ellwood and Hunter, 2000a; Ellwood and Hunter, 2000b; Hendry and Rickaby, 2008). That said, the Zn:Si ratio for *P. inermis* and *C. flexuosus* are consistent with field incubation measurements (Figs. 5 and 7). These differences likely result from species-specific Zn:Si values (e.g. *P. inermis* vs *C. flexuosus* vs *Thalassiosira psuedonana*). Southern Ocean sediments tend to be dominated by pennate diatoms such as *Fragilariopsis kerguelensis* and *Nitzschia* sp. and centric diatoms such as *Thalassiosira* sp., *Coscinodiscus* sp. and *Eucampia antarctica* (Armand et al., 2005; Crosta et al., 2005) thus the sedimentary Zn:Si ratio (range 1 to 10 μmol mol^{-1})(Andersen et al., 2011; Ellwood and Hunter, 1999, 2000b; Hendry and Rickaby, 2008) may vary depending on the relative composition of these species, although this remains to be tested.

Zinc isotope values for the frustule material obtained from the incubation experiment were heavier than the initial seawater composition for iron-limited treatments (Fig. 7). The zinc isotope signature approached the initial seawater composition for treatments with added iron. This is consistent with the culture experiments where the isotope composition of frustule material tended to light values at higher Fe' values (Figs. 4 and 7). It is well known that changes in iron bioavailability influences silicic acid uptake and frustule silicification in diatoms, which manifests through to changes in frustule size and silicon isotope composition (Leynaert et al., 2004; Meyerink et al., 2017a; Meyerink et al., 2017b). Increased zinc isotope fractionation between frustule and organic material ($\Delta^{66}Zn_{frustule\text{-}organic}$) for iron-replete cells is likely tied to increases in silicic uptake rate and frustule silicification, and not just zinc isotope fractionation associated with iron regulation of divalent metal transporters.

Recently Ellwood et al. (2020a) and Cloete et al. (2021) noted that zinc has a longer regeneration lengthscale to than of phosphorous, leading to an increase in the Zn:P ratio with depth. An increase in the Zn:P ratio is also observed for the SOTS, SS1 and SS2 stations (Fig. 8). When calculating the regeneration lengthscale, one needs to be mindful that the zinc content of the Southern Ocean diatom frustules appears to be a significant zinc sink (range 9–18% for culture experiments and 1–57% for the shipboard incubation experiment (Fig. 7)), which is much higher than the ~3% reported for the temperate diatom *T. psuedonana* (Ellwood and Hunter, 2000a). Additionally, zinc trapped within the frustule

would resist regeneration, leading to a higher deep water concentration that would not be present for phosphorous, increasing the regeneration lengthscale for zinc relative to that of phosphorous.

4.2. Zinc adsorption and δ^{66}Zn fractionation in the field incubation experiment

A potential explanation of the heavy $\Delta^{66}Zn_{organic\text{-}SW}$ values for the field incubation experiment (Fig. 7D) cells could be attributed to the adsorption of zinc on cell surfaces and the co-precipitation of zinc with iron oxy-hydroxides when cultures are grown at high iron concentrations (Gélabert et al., 2006; John et al., 2007; John and Conway, 2014). John and Conway (2014) demonstrated in a culture experiment employing the diatom *Dunalliela tertiolecta*, that isotopically heavier zinc could adsorb onto dead and degrading cells. In our field study, increased zinc isotope fractionation was observed in the incubation experiment for treatments with high concentrations of added iron (Fig. 7), which might be associated with zinc adsorption to surface iron oxy-hydroxides. It is also possible the heavy isotope signal seen in the cells without added zinc is due to a high utilisation rate of the dissolved zinc, increasing the isotopic signature. However, this effect was not seen as strongly in the samples with a small amount of added iron, which had a similar increase in growth rate (Fig. 7). Thus, the heavy signal could result from zinc being adsorbed onto the surface of particulate material within the incubation.

Another possible explanation for the heavy zinc isotope composition is for the release of light zinc from the cells as they senesce and die (Fig. 3). Additionally, the field incubation is likely to have grazers present that are also likely to help recycle zinc from biogenic material, again with the faster release of light zinc. These processes would lead to a heavier isotope composition of the cellular particulate zinc and a reduction in the cellular Zn:P ratio, as zinc is released back into the solution. This idea is relevant to the communities of phytoplankton that have high biomass and are in steady state growth, like those found at the end of large phytoplankton blooms.

The release of isotopically light zinc from particulate material is supported by the significant decline in the Zn:P composition of cells harvested in the steady-state phase of growth relative to cells harvested during the exponential phase of growth and their heavier isotope composition (Fig. 3). It also implies that in the open ocean, during the initial phase of the phytoplankton bloom, cells would tend to have a high Zn:P ratio with a lighter zinc isotope composition while the dissolved pool would become isotopically heavier. In contrast, after the peak of the bloom, the Zn:P ratio of particulate material would tend to decrease, and the zinc isotope composition would likely increase due to the presence of decaying organic matter, in addition to healthy cells, i.e. senescing and dead cells releasing isotopically lighter zinc (Fig. 3). The presence of senescing and decaying material would also enhance the amount of zinc being scavenged from solution. Thus, the Zn:P ratio and zinc isotope composition of the natural phytoplankton community may also depend on when they are sampled relative to bloom initiation.

The rapid regeneration of isotopically light particulate zinc in surface water was proposed by Vance et al. (2019). As mentioned above, in-situ studies on Zn:P ratio of particulates in the Southern Ocean reveal that particulate zinc may regenerate more slowly than particulate phosphorus (Cloete et al., 2021; Ellwood et al., 2020a), which would appear to contradict the idea that zinc is regenerated at a fast rate than that of phosphorous (Fig. 3)(Vance et al., 2019). We believe that this difference results from zinc bound within frustule silica not being regenerated on the same lengthscale as that of zinc within the organic tissue of diatoms, thus resulting in an increase in the Zn:P ratio with depth (Fig. 8).

4.3. Dissolved and particulate δ^{66}Zn depth profiles and oceanographic relevance

The SOTS, SS1, and SS2 sites all had active growing cells at the time of occupation in 2020/2021, with diatoms dominating the phytoplankton community. The Zn:P ratios for organic matter within the upper 100 m are similar to that of laboratory culture cells grown at a comparable free Zn^{2+} concentration, estimated from previously measured ligand concentrations for SAZ and Polar waters (Fig. 2B) (Baars and Croot, 2011; Ellwood, 2004; Sinoir et al., 2016). The isotope difference between the particulate and dissolved phase ($\Delta^{66}Zn_{part\text{-}diss}$) for the upper 100 m was 0.56 ± 0.24 ‰, -0.36 ± 0.14 ‰, -0.56 ± 0.30 ‰ for SOTS, SS1 and SS2, respectively.

The production of isotopically light particulate zinc in surface waters at the two polar sites is consistent with zinc uptake by phytoplankton. This is kinetically controlled, so particles are expected to be isotopically light relative to uncomplexed zinc. Scavenging also involves the removal of uncomplexed zinc (Sieber et al., 2023; Weber et al., 2018). Estimated free Zn^{2+} concentrations are about an order of magnitude higher for the two polar sites compared to the SOTS site. If scavenging was dominating at these two sites, the isotope composition of particulate zinc might be expected to be heavier than dissolved zinc, which was not observed (Fig. 8, S3, and S4). Rather, biological uptake appears to be the dominant process influencing the particulate isotope composition at these two sites.

Organic complexation of zinc can also influence the isotope composition of the dissolved pool. In culture experiments, the complexation of dissolved zinc by EDTA results in the free Zn^{2+} being isotopically lighter than complexed zinc ($\varepsilon_{ZnEDTA} \approx 0.33$ ‰) (Marković et al., 2017). However, the modelling efforts of Weber et al. (2018) and Sieber et al. (2023) require the isotope composition of ligand-bound zinc to be isotopically lighter ($\varepsilon_{ZnL} \approx -0.42$ ‰) than the unbound zinc pool. Across all three field sites, complexation by natural organic ligands is expected to be significant within the upper 100 m where dissolved zinc concentrations are <1 nmol kg^{-1} (Table S1), assuming ligand concentrations are similar to those determined for subantarctic and polar waters (range: 1.2 and 5.3 nmol L^{-1})(Baars and Croot, 2011; Ellwood, 2004). Assuming ligand complexation results in the free Zn^{2+} pool being isotopically heavy (as advocated by Weber et al. (2018) and Sieber et al. (2023)), this should result in positive $\Delta^{66}Zn_{part\text{-}diss}$ values. For the two polar sites, $\Delta^{66}Zn_{part\text{-}diss}$ values are negative, suggesting that zinc fractionation upon biological uptake dominates the signal.

In contrast to the two polar sites, $\Delta^{66}Zn_{part\text{-}diss}$ at the SOTS site was positive. The transition from lighter $\Delta^{66}Zn_{part\text{-}diss}$ values to heavier values, going from higher to lower zinc concentration waters, is consistent with our diatom $\Delta^{66}Zn_{organic\text{-}media}$ culture results (Fig. 1C, F, and S2) and previous culture work (John et al., 2007; Samanta et al., 2018). That said, if ε_{ZnL} is indeed negative, then ligand complexation would help to explain the heavier $\Delta^{66}Zn_{part\text{-}diss}$ value for the SOTS site. As mentioned, the challenge with ε_{ZnL} being negative is that laboratory experiments involving synthetic ligands indicated that ligand complexation should result in positive ε_{ZnL} values (Marković et al., 2017). The scavenging of uncomplexed zinc from the solution might also explain the observed positive $\Delta^{66}Zn_{part\text{-}diss}$ values. Finally, the loss of isotopically light zinc from sinking decaying organic material (Fig. 3) could result in heavier $\Delta^{66}Zn_{part\text{-}diss}$ values at SOTS. Clearly, more work is required to understand the fractionation processes and interactions between the dissolved and particulate pools.

The processes that influence the biogeochemical composition of surface waters of the Southern Ocean are reflected in other parts of the global ocean via water masses originating in this region (Sarmiento et al., 2004; Sieber et al., 2020; Vance et al., 2017; Weber et al., 2018; Zhao et al., 2014). These water masses include Subantarctic Mode Water (SAMW), Antarctic Intermediate Water (AAIW) and the Antarctic Bottom Water (AABW), which form in the Subantartic Zone (SAZ), the Polar Front Zone (PFZ) and near the Antarctic continental ice shelf of the Southern Ocean, respectively. Thus, the δ^{66}Zn composition of global water masses influenced by SAMW, AAIW and AABW will be affected by the δ^{66}Zn composition of surface waters in their formation regions (Roshan et al., 2018; Sieber et al., 2020; Vance et al., 2017; Weber et al.,

2018; Zhao et al., 2014).

Our diatom culture result shows that zinc isotope fractionation is strongly influenced by iron bioavailability, with isotope fractionation tending to be lighter for organic tissue values under iron limitation and heavier values under iron-replete conditions (Fig. 2). If applied to open ocean waters where iron bioavailability is low, this would result in the dissolved zinc pool becoming isotopically heavy, in contrast to the other processes that have been identified to result in heavier values (e.g. scavenging).

4.4. δ^{66}Zn composition of frustules

The work of Andersen et al. (2011) showed that the δ^{66}Zn isotope composition of sediment-bound diatom frustules tended to increase with decreasing zinc content. This is consistent with the incubation results for *C. flexuous* and *P. inermis* where zinc isotope composition increased as the free Zn^{2+} concentration and Zn:Si ratio decreased (Fig. 4). A potential reason for this is that zinc incorporation into frustules is kinetically controlled as is for organic tissue when zinc bioavailability is low (John et al., 2007; Samanta et al., 2018). Andersen et al. (2011) also found that the zinc isotope composition of diatom frustules is isotopically heavier than the average seawater isotope composition. The results from the field incubation are consistent with the findings of Andersen et al. (2011), where the low zinc treatments are isotopically heavy compared to the initial seawater isotope composition (Fig. 7E). Our findings confirm the Zn:Si ratio and the zinc isotope composition of diatom opal are useful for tracing zinc bioavailability with the caveat that changes in iron bioavailability can also influence these two parameters (Fig. 4C and F).

Finally, this work has implications for the global ocean zinc budget. Globally, biogenic silica burial flux associated with diatoms totals ~6.3 $\pm$ 3.6 $\times$ 10^{12} mol y^{-1} (Tréguer and De La Rocha, 2013). Using a Zn:Si ratio of 3 to 590 μmol:mol from this work and previous studies would result in a zinc burial flux ranging between 1.9 $\times$ 10^{7} mol y^{-1} and 3.7 $\times$ 10^{9} mol y^{-1}. This large range in burial flux values highlights that zinc burial associated with biogenic silica might be substantial - current organic zinc burial fluxes range from 9.67 $\times$ 10^{7} mol y^{-1} to 4.8 $\times$ 10^{8} mol y^{-1} (Dickson, 2022) - but clearly, these flux estimates are subject to an appropriate Zn:Si value for diatom frustules. The zinc isotope composition of buried silica is expected to be similar to or lighter than organic matter (−0.3 to −0.8 ‰; e.g. Fig. 4F for no and low iron additions). The Zn:Si ratios obtained for *P. inermis, C. flexuosus* and the field incubation experiments grown at relevant ranges for Zn^{2+} for the Southern Ocean, thus the oceanic budget may need to consider of the role diatoms play in zinc loss from the ocean. The uptake and incorporation of zinc into the frustules of Southern Ocean diatoms also needs to be reconsidered as this may be important in the biogeochemical coupling of the zinc and silicon in the ocean along with the leakage of isotopically light waters from the SAZ to low latitudes via subantarctic mode water.

5. Conclusions

Iron limitation was shown to have a drastic effect on the Zn:P ratio of phytoplankton, whereby the Zn:P ratio increased with an increasing degree of limitation. These changes are likely related to the induction of iron reduction processes by the iron-starved cells and the expression of divalent metal transporters to aid iron acquisition. A comparison between the exponential and steady-state harvested cells revealed that zinc is more labile than that of phosphorus during cellular regeneration, thus resulting in a decline in the cellular Zn:P ratio. Coupled with this was a significant change in the zinc isotope composition of cells, with cellular zinc isotope composition becoming heavier with an increasing degree of iron limitation. For our two diatoms *P. inermis* and *C. flexuosus,* we noted that the Zn:Si ratio content of their frustules increased with increasing Zn^{2+} concentration and the degree of iron limitation. The upregulation of zinc acquisition under iron limiting conditions likely resulted in the increased Zn:Si ratios for frustules. The percentage of zinc associated with the frustule ranged between 9 and 13% for culture diatoms and up to 50% for cells incubated in the field experiment – much higher than previous estimates at 3%. The depth profiles of dissolved and particulate zinc concentration and isotope composition vary; at the SOTS site, dissolved zinc was isotopically light relative to particulate zinc, while at two Polar stations, dissolved zinc was isotopically heavier than particulate zinc. This work shows that biogenic opal is a more significant removal vector of zinc from the surface ocean than previously thought, which has implications for the biogeochemical coupling of zinc and silicon in the global ocean. This work also indicated that iron plays a pivotal role in regulating zinc uptake by phytoplankton and the isotope of dissolved zinc in the surface ocean.

Author contributions

RG, MS and MJE conceived the project; RG undertook the work and sample analysis, and all authors contributed to writing the manuscript.

Declaration of Competing Interest

None.

Data availability

Data will be made available on request.

Acknowledgments

The Australian Centre for Excellence in Antarctic Science is a Special Research Initiative funded by the Australian Research Council (SR200100008). Financial support for this work came from the Australian Research Council (DP170102108 and DP220100289). RSES and ANU scholarships to Robin Grun and Moneesha Samanta are also acknowledged. The Australian Antarctic Program Partnership (AAPP) for supporting the IN2020_V08 voyage. Ship time for this research was financially supported by Australia's Marine National Facility. The authors are grateful to the officers, crew, and research staff of the Marine National Facility and the *R.V.* Investigator for their help with sample collection and generation of hydrochemistry data on voyages IN2019_V02 and IN2020_V08. The authors wish to thank Chief Scientist Philip Boyd for allowing the ANU Team to be part of the IN2020_V08 voyage. We thank the comments from two reviewers that helped to improve the manuscript.

Appendix A. Supplementary data

Supplementary data to this article can be found online at https://doi.org/10.1016/j.marchem.2023.104330.

References

Andersen, M.B., Vance, D., Archer, C., Anderson, R.F., Ellwood, M.J., Allen, C.S., 2011. The Zn abundance and isotopic composition of diatom frustules, a proxy for Zn availability in ocean surface seawater. Earth Planet. Sci. Lett. 301, 137–145.

Andrew, S.M., Morell, H.T., Strzepek, R.F., Boyd, P.W., Ellwood, M.J., 2019. Iron availability influences the tolerance of Southern Ocean phytoplankton to warming and elevated irradiance. Front. Mar. Sci. 6, 1–12.

Andrew, S.M., Strzepek, R.F., Branson, O., Ellwood, M.J., 2022. Ocean acidification reduces the growth of two Southern Ocean phytoplankton. Mar. Ecol. Prog. Ser. 682, 51–64.

Archer, C., Andersen, M.B., Cloquet, C., Conway, T.M., Dong, S., Ellwood, M., Moore, R., Nelson, J., Rehkamper, M., Rouxel, O., Samanta, M., Shin, K.-C., Sohrin, Y., Takano, S., Wasylenki, L., 2017. Inter-calibration of a proposed new primary reference standard AA-ETH Zn for zinc isotopic analysis. J. Anal. At. Spectrom 32, 415–419.

Armand, L.K., Crosta, X., Romero, O., Pichon, J.J., 2005. The biogeography of major diatom taxa in Southern Ocean sediments: 1. Sea ice related species. Palaeogeography, Palaeoclimatology, Palaeoecology 223, 93–126.

Baars, O., Croot, P.L., 2011. The speciation of dissolved zinc in the Atlantic sector of the Southern Ocean. Deep Sea Res. Pt II 58, 2720–2732.
Ban, Y., Aida, M., Nomura, M., Fujii, Y., 2002. Zinc isotope separation by ligand exchange chromatography using cation exchange resin. J. Ion Exch. 13, 46–52.
Blaby-Haas, C.E., Merchant, S.S., 2017. Regulating cellular trace metal economy in algae. Curr. Opin. Plant Biol. 39, 88–96.
Boyd, P.W., Ellwood, M.J., 2010. The biogeochemical cycle of iron in the ocean. Nat. Geosci. 3, 675–682.
Boyd, P.W., Watson, A.J., Law, C.S., Abraham, E.R., Trull, T., Murdoch, R., Bakker, D.C. E., Bowie, A.R., Buesseler, K.O., Chang, H., Charette, M., Croot, P., Downing, K., Frew, R., Gall, M., Hadfield, M., Hall, J., Harvey, M., Jameson, G., LaRoche, J., Liddicoat, M., Ling, R., Maldonado, M.T., McKay, R.M., Nodder, S., Pickmere, S., Pridmore, R., Rintoul, S., Safi, K., Sutton, P., Strzepek, R., Tanneberger, K., Turner, S., Waite, A., Zeldis, J., 2000. A mesoscale phytoplankton bloom in the polar Southern Ocean stimulated by iron fertilization. Nature 407, 695–702.
Boyd, P., Crossley, A., DiTullio, G., Griffiths, F., Hutchins, D., Queguiner, B., Sedwick, P., Trull, T., 2001. Control of phytoplankton growth by iron supply and irradiance in the subantarctic Southern Ocean: experimental results from the SAZ project. J. Geophys. Res. 106, 531–573.
Boyd, P., Antoine, D., Baldry, K., Cornec, M., Ellwood, M., Halfter, S., Lacour, L., Latour, P., Strzepek, R., Trull, T., Rohr, T., 2023. Controls on Polar Southern Ocean Deep Chlorophyll Maxima: Viewpoints from Multiple Observational Platforms.
Bruland, K.W., Knauer, G.A., Martin, J.H., 1978. Zinc in north-East Pacific water. Nature 271, 741–743.
Cloete, R., Loock, J.C., van Horsten, N.R., Menzel Barraqueta, J.L., Fietz, S., Mtshali, T. N., Planquette, H., García-Ibáñez, M.I., Roychoudhury, A.N., 2021. Winter dissolved and particulate zinc in the Indian sector of the Southern Ocean: distribution and relation to major nutrients (GEOTRACES GIpr07 transect). Mar. Chem. 236, 104031.
Coale, K.H., Johnson, K.S., Chavez, F.P., Buesseler, K.O., Barber, R.T., Brzezinski, M.A., Cochlan, W.P., Millero, F.J., Falkowski, P.G., Bauer, J.E., Wanninkhof, R.H., Kudela, R.M., Altabet, M.A., Hales, B.E., Takahashi, T., Landry, M.R., Bidigare, R.R., Wang, X., Chase, Z., Strutton, P.G., Friederich, G.E., Gorbunov, M.Y., Lance, V.P., Hilting, A.K., Hiscock, M.R., Demarest, M., Hiscock, W.T., Sullivan, K.F., Tanner, S. J., Gordon, R.M., Hunter, C.N., Elrod, V.A., Fitzwater, S.E., Jones, J.L., Tozzi, S., Koblizek, M., Roberts, A.E., Herndon, J., Brewster, J., Ladizinsky, N., Smith, G., Cooper, D., Timothy, D., Brown, S.L., Selph, K.E., Sheridan, C.C., Twining, B.S., Johnson, Z.I., 2004. Southern Ocean iron enrichment experiment: carbon cycling in high- and low-Si waters. Science 304, 408–414.
Coale, T.H., Moosburner, M., Horák, A., Oborník, M., Barbeau, K.A., Allen, A.E., 2019. Reduction-dependent siderophore assimilation in a model pennate diatom. Proc. Natl. Acad. Sci. U. S. A. 116, 23609–23617.
Collier, R., Edmond, J., 1984. The trace element geochemistry of marine biogenic particulate matter. Prog. Oceanogr. 13, 113–199.
Conway, T.M., John, S.G., 2014. The biogeochemical cycling of zinc and zinc isotopes in the North Atlantic Ocean. Global Biogeochem. Cycles 28, 1111–1128, 2014GB004862.
Criss, R.E., 1999. Principles of Stable Isotope Distribution. Oxford University Press, New York.
Crosta, X., Romero, O., Armand, L.K., Pichon, J.J., 2005. The biogeography of major diatom taxa in Southern Ocean sediments: 2. Open Ocean related species. Palaeogeogr. Palaeoclimatol. Palaeoecol. 223, 66–92.
Cullen, J.T., Chase, Z., Coale, K.H., Fitzwater, S.E., Sherrell, R.M., 2003. Effect of iron limitation on the cadmium to phosphorus ratio of natural phytoplankton assemblages from the Southern Ocean. Limnol. Oceanogr. 48, 1079–1087.
de Souza, G.F., Khatiwala, S.P., Hain, M.P., Little, S.H., Vance, D., 2018. On the origin of the marine zinc–silicon correlation. Earth Planet. Sci. Lett. 492, 22–34.
Deppeler, S.L., Davidson, A.T., 2017. Southern ocean phytoplankton in a changing climate. Frontiers in Marine Science 4.
Dickson, A.J., 2022. The zinc isotope composition of late Holocene open-ocean marine sediments. Chem. Geol. 605, 120971.
Ding, X., Nomura, M., Fujii, Y., 2010. Zinc isotope effects by chromatographic chelating exchange resin. Prog. Nucl. Energy 52, 164–167.
Druce, M., Stirling, C.H., Rolison, J.M., 2020. High-precision zinc isotopic measurement of certified reference materials relevant to the environmental, earth, planetary and biomedical sciences. Geostand. Geoanal. Res. 44, 711–732.
Ellwood, M.J., 2004. Zinc and cadmium speciation in subantarctic waters east of New Zealand. Mar. Chem. 87, 37–58.
Ellwood, M.J., Hunter, K.A., 1999. Determination of the Zn/Si ratio in diatom opal: a method for the separation, cleaning and dissolution of diatoms. Mar. Chem. 66, 149–160.
Ellwood, M.J., Hunter, K.A., 2000a. The incorporation of zinc and iron into the frustule of the marine diatom *Thalassiosira pseudonana*. Limnol. Oceanogr. 45, 1517–1524.
Ellwood, M.J., Hunter, K.A., 2000b. Variations in the Zn/Si record over the last interglacial glacial transition. Paleoceanography 15, 506–514.
Ellwood, M.J., Strzepek, R., Chen, X., Trull, T.W., Boyd, P.W., 2020a. Some observations on the biogeochemical cycling of zinc in the Australian sector of the Southern Ocean: a dedication to Keith Hunter. Mar. Freshw. Res. 71, 355–373.
Ellwood, M.J., Strzepek, R.F., Strutton, P.G., Trull, T.W., Fourquez, M., Boyd, P.W., 2020b. Distinct iron cycling in a Southern Ocean eddy. Nat. Commun. 11, 1–8.
Eriksen, R., Trull, T.W., Davies, D., Jansen, P., Davidson, A.T., Westwood, K., van den Enden, R., 2018. Seasonal succession of phytoplankton community structure from autonomous sampling at the Australian Southern Ocean time series (SOTS) observatory. Mar. Ecol. Prog. Ser. 589, 13–31.
Gélabert, A., Pokrovsky, O.S., Viers, J., Schott, J., Boudou, A., Feurtet-Mazel, A., 2006. Interaction between zinc and freshwater and marine diatom species: surface complexation and Zn isotope fractionation. Geochim. Cosmochim. Acta 70, 839–857.
Graham, R.M., De Boer, A.M., van Sebille, E., Kohfeld, K.E., Schlosser, C., 2015. Inferring source regions and supply mechanisms of iron in the Southern Ocean from satellite chlorophyll data. Deep Sea Res. Pt I 104, 9–25.
Hendry, K.R., Rickaby, R.E.M., 2008. Opal (Zn/Si) ratios as a nearshore geochemical proxy in coastal Antarctica. Paleoceanography 23. https://doi.org/10.1029/2007PA001576.
Hernlem, B.J., Vane, L.M., Sayles, G.D., 1996. Stability constants for complexes of the siderophore desferrioxamine B with selected heavy metal cations. Inorg. Chim. Acta 244, 179–184.
Jeong, H., Ra, K., Choi, J.Y., 2021. Copper, zinc and Lead Isotopic Delta values and isotope ratios of various geological and biological reference materials. Geostand. Geoanal. Res. 45, 551–563.
John, S.G., Conway, T.M., 2014. A role for scavenging in the marine biogeochemical cycling of zinc and zinc isotopes. Earth Planet. Sci. Lett. 394, 159–167.
John, G.S., Geis, R.W., Saito, M.A., Boyle, E.A., 2007. Zinc isotope fractionation during high-affinity and low-affinity zinc transport by the marine diatom Thalassiosira oceanica. Limnol. Oceanogr. 52, 2710–2714.
Köbberich, M., Vance, D., 2017. Kinetic control on Zn isotope signatures recorded in marine diatoms. Geochim. Cosmochim. Acta 210, 97–113.
Köbberich, M., Vance, D., 2019. Zn isotope fractionation during uptake into marine phytoplankton: implications for oceanic zinc isotopes. Chem. Geol. 523, 154–161.
Koch, F., Trimborn, S., 2019. Limitation by Fe, Zn, Co, and B12 results in similar physiological responses in two antarctic phytoplankton species. Frontiers in Marine Science 6.
Latour, P., Strzepek, R.F., Wuttig, K., Merwe, P.V.D., Eggins, S., Bach, L.T., Boyd, P.W., Ellwood, M.J., Pinfold, T.L., Bowie, A.R., 2022. Seasonality of phytoplankton growth limitation by iron and manganese in subantarctic waters. Earth and Space Science Open Archive 26.
Leynaert, A., Bucciarelli, E., Claquin, P., Dugdale, R.C., Martin-Jezequel, V., Pondaven, P., Ragueneau, O., 2004. Effect of iron deficiency on diatom cell size and silicic acid uptake kinetics. Limnol. Oceanogr. 49, 1134–1143.
Lis, H., Shaked, Y., Kranzler, C., Keren, N., Morel, F.M.M., 2015. Iron bioavailability to phytoplankton: an empirical approach. ISME J. 9, 1003–1013.
Maldonado, M.T., Strzepek, R.F., Sander, S., Boyd, P.W., 2005. Acquisition of iron bound to strong organic complexes, with different Fe binding groups and photochemical reactivities, by plankton communities in Fe-limited subantarctic waters. Global Biogeochem. Cycles 19.
Marković, T., Manzoor, S., Humphreys-Williams, E., Kirk, G.J.D., Vilar, R., Weiss, D.J., 2017. Experimental determination of zinc isotope fractionation in complexes with the Phytosiderophore 2′-Deoxymugeneic acid (DMA) and its structural analogues, and implications for plant uptake mechanisms. Environ. Sci. Technol. 51, 98–107.
Meyerink, S., Ellwood, M.J., Maher, W.A., Strzepek, R., 2017a. Iron availability influences silicon isotope fractionation in two Southern Ocean diatoms (*Proboscia inermis* and *Eucampia antarctica*) and a coastal diatom (*Thalassiosira pseudonana*). Frontiers in marine. Science 4.
Meyerink, S.W., Ellwood, M.J., Maher, W.A., Dean Price, G., Strzepek, R.F., 2017b. Effects of iron limitation on silicon uptake kinetics and elemental stoichiometry in two Southern Ocean diatoms, *Eucampia antarctica* and *Proboscia inermis*, and the temperate diatom *Thalassiosira pseudonana*. Limnol. Oceanogr. 62, 2445–2462.
Morel, F.M.M., Reinfelder, J.R., Roberts, S.B., Chamberlain, C.P., Lee, J.G., Yee, D., 1994. Zinc and carbon co-limitation of marine phytoplankton. Nature 369, 740–742.
Moreno, C.M., Gong, W., Cohen, N.R., DeLong, K., Marchetti, A., 2020. Interactive effects of iron and light limitation on the molecular physiology of the Southern Ocean diatom Fragilariopsis kerguelensis. Limnol. Oceanogr. 65, 1511–1531.
Price, N.M., Harrison, G.I., Hering, J.G., Hudson, R.J., Nirel, P.M.V., Palenik, B., Morel, F.M.M., 1988. Preparation and chemistry of the artificial algal culture medium Aquil. Biol. Oceanogr. 6, 443–461.
Rintoul, S.R., 2018. The global influence of localized dynamics in the Southern Ocean. Nature 558, 209–218.
Roshan, S., DeVries, T., Wu, J., Chen, G., 2018. The internal cycling of zinc in the ocean. Global Biogeochem. Cycles 32, 1833–1849.
Samanta, M., Ellwood, M.J., Sinoir, M., Hassler, C.S., 2017. Dissolved zinc isotope cycling in the Tasman Sea, SW Pacific Ocean. Mar. Chem. 192, 1–12.
Samanta, M., Ellwood, M.J., Strzepek, R.F., 2018. Zinc isotope fractionation by *Emiliania huxleyi* cultured across a range of free zinc ion concentrations. Limnol. Oceanogr. 63, 660–671.
Sarmiento, J.L., Gruber, N., Brzezinski, M.A., Dunne, J.P., 2004. High-latitude controls of thermocline nutrients and low latitude biological productivity. Nature 427, 56–60.
Sedwick, P.N., DiTullio, G.R., Hutchins, D.A., Boyd, P.W., Griffiths, F.B., Crossley, A.C., Trull, T.W., Queguiner, B., 1999. Limitation of algal growth by iron deficiency in the Australian Subantarctic region. Geophys. Res. Lett. 26, 2865–2868.
Shaked, Y., Kustka, A.B., Morel, F.M.M., 2005. A general kinetic model for iron acquisition by eukaryotic phytoplankton. Limnol. Oceanogr. 50, 872–882.
Sieber, M., Conway, T.M., de Souza, G.F., Hassler, C.S., Ellwood, M.J., Vance, D., 2020. Cycling of zinc and its isotopes across multiple zones of the Southern Ocean: insights from the Antarctic circumnavigation expedition. Geochim. Cosmochim. Acta 268, 310–324.
Sieber, M., Lanning, N.T., Bian, X., Yang, S.-C., Takano, S., Sohrin, Y., Weber, T.S., Fitzsimmons, J.N., John, S.G., Conway, T.M., 2023. The importance of reversible scavenging for the marine Zn cycle evidenced by the distribution of zinc and its isotopes in the Pacific Ocean. J. Geophys. Res. Oceans 128, e2022JC019419.
Sinoir, M., Ellwood, M.J., Butler, E.C.V., Bowie, A.R., Mongin, M., Hassler, C.S., 2016. Zinc cycling in the Tasman Sea: distribution, speciation and relation to phytoplankton community. Mar. Chem. 182, 25–37.

Strickland, J.D., Parsons, T.R., 1972. A Practical Handbook of Seawater Analysis.
Strzepek, R.F., Maldonado, M.T., Hunter, K.A., Frew, R.D., Boyd, P.W., 2011. Adaptive strategies by Southern Ocean phytoplankton to lessen iron limitation: uptake of organically complexed iron and reduced cellular iron requirements. Limnol. Oceanogr. 56, 1983–2002.
Sunda, W.G., Huntsman, S.A., 1992. Feedback interactions between zinc and phytoplankton in seawater. Limnol. Oceanogr. 37, 25–40.
Sunda, W., Huntsman, S., 2003. Effect of pH, light, and temperature on Fe–EDTA chelation and Fe hydrolysis in seawater. Mar. Chem. 84, 35–47.
Tréguer, P.J., De La Rocha, C.L., 2013. The World Ocean silica cycle. Ann. Rev. Mar. Sci. 5, 477–501.
Twining, B.S., Baines, S.B., 2013. The trace metal composition of marine phytoplankton. Ann. Rev. Mar. Sci. 5, 191–215.
Vance, D., Little, S.H., de Souza, G.F., Khatiwala, S., Lohan, M.C., Middag, R., 2017. Silicon and zinc biogeochemical cycles coupled through the Southern Ocean. Nat. Geosci. 10, 202–206.
Vance, D., de Souza, G.F., Zhao, Y., Cullen, J.T., Lohan, M.C., 2019. The relationship between zinc, its isotopes, and the major nutrients in the north-East Pacific. Earth Planet. Sci. Lett. 525, 115748.
Wang, R.M., Archer, C., Bowie, A.R., Vance, D., 2019. Zinc and nickel isotopes in seawater from the Indian sector of the Southern Ocean: the impact of natural iron fertilization versus Southern Ocean hydrography and biogeochemistry. Chem. Geol. 511, 452–464.
Weber, T., John, S., Tagliabue, A., DeVries, T., 2018. Biological uptake and reversible scavenging of zinc in the global ocean. Science 361, 72–76.
Xu, Y., Shi, D., Aristilde, L., Morel, F.M.M., 2012. The effect of pH on the uptake of zinc and cadmium in marine phytoplankton: possible role of weak complexes. Limnol. Oceanogr. 57, 293–304.
Ye, N., Han, W., Toseland, A., Wang, Y., Fan, X., Xu, D., van Oosterhout, C., Aslam, S.N., Barry, K., Beszteri, B., Brussaard, C., Clum, A., Copeland, A., Daum, C., Duncan, A., Eloe-Fadrosh, E., Fong, A., Foster, B., Foster, B., Ginzburg, M., Huntemann, M., Ivanova, N.N., Kyrpides, N.C., Martin, K., Moulton, V., Mukherjee, S., Palaniappan, K., Reddy, T.B.K., Roux, S., Schmidt, K., Strauss, J., Timmermans, K., Tringe, S.G., Underwood, G.J.C., Valentin, K.U., van de Poll, W.H., Varghese, N., Grigoriev, I.V., Tagliabue, A., Zhang, J., Zhang, Y., Ma, J., Qiu, H., Li, Y., Zhang, X., Mock, T., Sea of Change, C, 2022. The role of zinc in the adaptive evolution of polar phytoplankton. Nature Ecology & Evolution 6, 965–978.
Zhao, Y., Vance, D., Abouchami, W., de Baar, H.J.W., 2014. Biogeochemical cycling of zinc and its isotopes in the Southern Ocean. Geochim. Cosmochim. Acta 125, 653–672.